

# Chapter 3

## Parameterisation of the inner detector performance

### Contents

---

<b>3.1 Introduction .....</b>	<b>33</b>
<b>3.2 Detector simulation .....</b>	<b>34</b>
3.2.1 Full detector simulation .....	34
3.2.2 Fast detector simulation .....	34
<b>3.3 The smearing of track parameters in the inner detector.....</b>	<b>35</b>
3.3.1 Track parameters in the inner detector.....	35
3.3.2 The smearing of the track parameters .....	37
<b>3.4 Calculation of covariance matrices for the inner detector .....</b>	<b>39</b>
3.4.1 Introduction.....	39
3.4.2 Detector model.....	39
3.4.3 Derivation of the covariance matrix .....	42
<b>3.5 The <math>A \oplus B</math>-model.....</b>	<b>46</b>
<b>3.6 Resolutions and correlations for the inner detector.....</b>	<b>46</b>
3.6.1 Introduction.....	46
3.6.2 Transverse impact parameter resolution .....	46
3.6.3 Longitudinal impact parameter resolution .....	48
3.6.4 Azimuthal resolution.....	48
3.6.5 Polar angle resolution .....	50
3.6.6 Inverse transverse momentum resolution .....	51
3.6.7 Correlations.....	53
3.6.8 Conclusions.....	55
<b>3.7 Combined system inverse momentum resolution.....</b>	<b>55</b>
3.7.1 Calculation of the muon spectrometer inverse momentum resolution .....	55
3.7.2 Inverse momentum resolution for the muon spectrometer .....	56
3.7.3 Inverse momentum resolution for the combined system .....	59
<b>3.8 Muon charge identification performance .....</b>	<b>60</b>
<b>3.9 Principle of the description of tails .....</b>	<b>63</b>
<b>3.10 Conclusions and further work .....</b>	<b>64</b>
<b>3.11 References .....</b>	<b>65</b>

---

### 3.1 Introduction

In this chapter I present a parameterisation of the track reconstruction performance of the ATLAS inner detector. This parameterisation is implemented as a set of FORTRAN subroutines and functions, described in [1], and is currently used in the software package

ATLFAST [2]. The inner detector parameterisation is also implemented as a set of C++ classes, currently used in the package ATLFAST++ [3].

Section 3.2 describes the difference between full detector simulation and fast detector simulation based on parameterisation together with the advantages and restrictions of parametric detector simulation compared to full detector simulation. In a parametric detector simulation, for a given set of track parameters, describing the track in the magnetic field of the inner detector, a smeared set of track parameters is calculated, as would be determined from real measurements. The method used for smearing is based on a covariance matrix and described in more detail in section 3.3. The method used to calculate the covariance matrices for the inner detector is given in section 3.4. A simplified model for the calculation of the covariance matrices, the  $A \oplus B$ -model, is described in section 3.5. In section 3.6 I present the resolutions and correlations calculated with the parameterisation, and compare them with the  $A \oplus B$ -model and with the inner detector parameterisation implemented in the original version of ATLFAST. I have also used the parameterisation to make a study of the transverse momentum resolution of the combined inner detector/muon spectrometer system and of the muon spectrometer only. This study is presented in section 3.7. The muon charge identification performance of the ATLAS detector, which follows directly from the inverse transverse momentum resolution, is presented in section 3.8. A possible method to include non-Gaussian tails in the parameterisation is finally shortly described in section 3.9. The conclusions and further work are finally given in section 3.10.

## 3.2 Detector simulation

### 3.2.1 Full detector simulation

For many ATLAS studies, a simulation of the response of the ATLAS detector on particles passing through it is necessary. The FORTRAN packages GEANT [4] and DICE [5] provide such a simulation. GEANT is a package for the tracking of particles through detectors. The influence of the magnetic field, ionisation energy losses, multiple scattering, bremsstrahlung energy losses, photon conversions, nuclear interactions of hadrons and the decay of long-lived particles are taken into account. The package DICE (**D**etector **I**ntegration **C**ode) provides an accurate geometrical description of the ATLAS detector and an interface to GEANT. DICE provides also the simulation of the electronic response of the detector to particles. The response is obtained in a form similar to that which might be expected from the readout electronics after formatting by the online computers. Channel numbers, times, energies etc. are all stored. This relies on having an accurate model of the physical processes by which signals are collected and transformed by the readout electronics. The FORTRAN package XKALMAN [6] provides an algorithm for the reconstruction of tracks from the measured detector signals and the calculation of parameters of the reconstructed tracks. Detector simulation based on GEANT and DICE, eventually combined with track reconstruction, is also referred to as **full detector simulation**.

### 3.2.2 Fast detector simulation

A serious drawback of full detector simulation is that it is extremely complex and consumes much computer time. For this reason the FORTRAN package ATLFAST has been developed. This package provides a fast simulation of the (global) response of the ATLAS detector based on parameterisation. In a parametric detector simulation for each track a smeared track is calculated, describing the track actually measured, see also section 3.3. Parametric detector simulation always includes track reconstruction. Parametric detector simulation is dramati-

cally faster than full detector simulation. The calculation of the response of the ATLAS detector for a typical SUSY event takes with ATLFast less than 1 s, with full detector simulation 1-3 hours, depending on the computer platform used [7]. Detector simulation based on parameterisation is also referred to as **fast detector simulation**.

A serious restriction of fast detector simulation is that it is only suited for the simulation of the global response of the ATLAS detector (e.g. missing transverse energy, multiplicity of leptons and jets) and that it is only suited for a restricted set of physics studies. The package ATLFast is mainly developed for SUSY studies described in more detail in the next chapter. In particular, fast detector simulation can not be used for performance studies of track reconstruction algorithms.

### 3.3 The smearing of track parameters in the inner detector

#### 3.3.1 Track parameters in the inner detector

A set of five helix parameters  $\mathbf{p}$  can describe a track in the solenoidal magnetic field  $B$  of the inner detector:

$$\mathbf{p} = (a_0, z_0, \phi_0, \cot\theta, Q/p_T) \quad (3.1)$$

The five track parameters  $\mathbf{p}$  can be calculated directly from the momentum vector  $\vec{p}$  and position vector  $\vec{x}_v$  of the production vertex (appendix C). The parameters  $a_0$ ,  $z_0$ ,  $\phi_0$  and  $\cot\theta$  are shown in figure 3.1 and figure 3.2. The “true vertex” indicates the position where the track has been created.

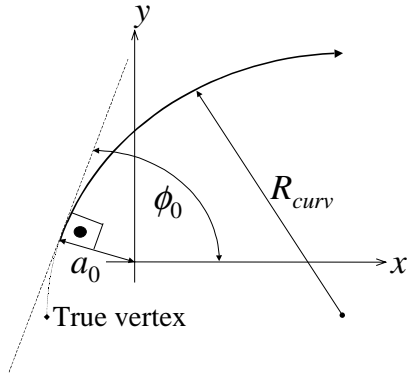


**Figure 3.1** The track parameters  $a_0$  and  $\phi_0$  in the  $(x, y)$  plane.

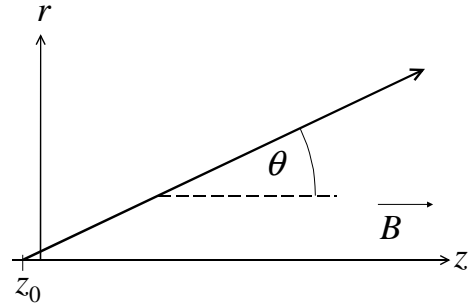


**Figure 3.2** The track parameters  $z_0$  and  $\cot\theta$  in the  $(r, z)$  plane. The direction of the magnetic field  $B$  is along the positive  $z$ -axis.

#### Impact parameters

The transverse impact parameter  $a_0$  is defined as the distance of closest approach to the beam-line. The sign of  $a_0$  is negative if the track has positive angular momentum around the beam line. Figure 3.3 shows the four cases where the absolute values of the transverse impact parameter are all the same and only the sign differs:

1. Positively charged particle, transverse impact parameter positive;
2. Negatively charged particle, transverse impact parameter positive;
3. Positively charged particle, transverse impact parameter negative;
4. Negatively charged particle, transverse impact parameter negative;

The longitudinal impact parameter  $z_0$  is defined as the value of  $z$  of the point on the track that determines  $a_0$ .

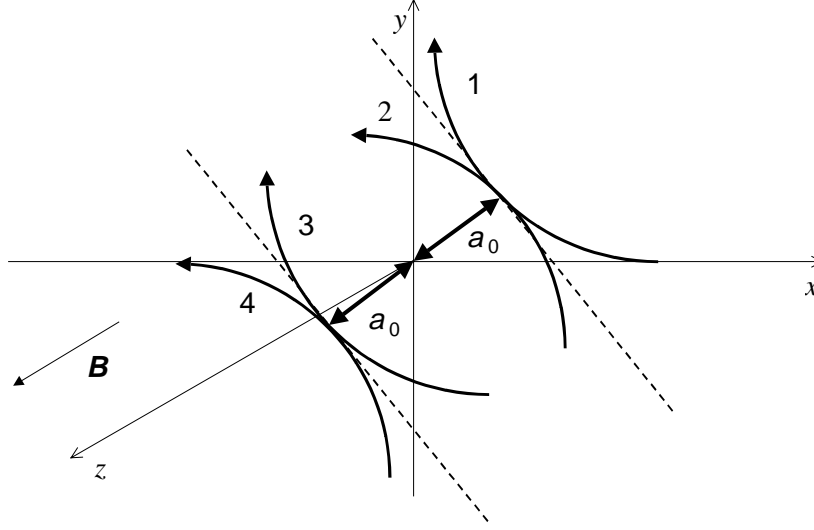


**Figure 3.3** Tracks (projected onto the  $(x, y)$  plane) of a particle with positive/negative charge and positive/negative impact parameter. The magnetic field direction is along the positive  $z$ -axis.

#### Angular co-ordinates

The angular co-ordinates are  $\phi_0$  and  $\cot\theta$ . The parameter  $\phi_0$  is the azimuth (the angle between the direction of motion of the track in the  $(x, y)$  plane and the  $x$ -axis) at the point of closest approach. The parameter  $\cot\theta$ , with  $\theta$  the polar angle, gives the inverse slope of the track in the  $(r, z)$  plane. The pseudorapidity  $\eta$ , introduced in section 1.3, is directly related to  $\cot\theta$  via  $\eta = \text{asinh}(\cot\theta)$  or  $\eta = -\ln(\tan(\theta/2))$ .

#### Inverse transverse momentum

The inverse transverse momentum  $Q/p_T$ , with  $Q$  the charge of the particle, can be deduced from the measured radius of curvature  $R_{\text{curv}}$ . This means that  $Q/p_T$ , and not  $p_T$ , is the quantity measured with Gaussian errors. The relation between  $Q/p_T$  and the radius of curvature  $R_{\text{curv}}$  (see figure 3.1) of the track in the magnetic field  $B$  is given by:

$$\frac{Q[\text{e}]}{p_T[\text{GeV}]} = \frac{1}{0.3 \cdot B[\text{T}] \cdot R_{\text{curv}}[\text{m}]} \quad (3.2)$$

#### Covariance matrix

Because the errors on the five track parameters are not independent, they are described by a  $5 \times 5$  covariance matrix  $C$ . The diagonal elements are the squared sigma values  $C_{aa} = \text{cov}(p_a) = \sigma_a^2$ . The off-diagonal terms are  $C_{ab} = \text{cov}(p_a, p_b) = \rho_{ab}\sigma_a\sigma_b$ , with  $\rho_{ab}$  the correlation between parameter  $p_a$  and parameter  $p_b$  ( $|\rho_{ab}| \leq 1$ ). If  $p_a$  and  $p_b$  are independent  $\rho_{ab} = 0$ . If  $p_a$  and  $p_b$  are linearly related  $|\rho_{ab}| = 1$ . Because in a very good approximation the variables in the  $(x, y)$  plane and the  $(r, z)$  plane are independent, only  $2 \times 4$  covariances are not zero<sup>1</sup>:  $\text{cov}(Q/p_T, \phi_0)$ ,  $\text{cov}(Q/p_T, a_0)$ ,  $\text{cov}(\phi_0, a_0)$  and  $\text{cov}(\cot\theta, z_0)$ . Covariance matrices are always symmetric, invertible and **positive definite**. Positive definite means that for each vector  $t$ :

$$\sum_{i=1}^5 \sum_{j=1}^5 C_{ij} t_i t_j > 0 \quad (3.3)$$

#### 3.3.2 The smearing of the track parameters

In a parametric detector simulation, a smeared set of track parameters  $p$  is calculated from a given set of track parameters  $\hat{p}$ . The smeared set describes the track parameters actually measured. In the current ATLFAST implementation, the smearing is based on a set of five correlated double precision random numbers generated according to a covariance matrix, using double precision versions of the standard CERN library routines RNORML, CORGEN and CORSET [8]. The routine CORGEN generates vectors of random numbers in a Gaussian distribution of mean zero and covariance matrix  $C$  using the Gaussian random number generator RNORML. The generator must first be set up by a call to CORSET that transforms the covariance matrix  $C$  to an appropriate so-called *square root* matrix  $c$  that is then used by CORGEN.

The covariance matrix used for the smearing depends on the particle type and the incoming track parameters (actually  $Q/p_T$  and  $\eta$ ). Four different charged particle types are distinguished in ATLFAST: electrons, muons, primary pions and secondary pions (created in the decay of  $K_S^0$  mesons). All other charged particles are treated as primary pions.

#### Smearing of muon track parameters

In the case of muons, a single Gaussian distribution can describe the distribution of the resolution of each track parameter  $\hat{p}_i$ . The contribution of tails in the distribution is negligible [9]. Hence smeared track parameters  $p_i$  are determined by using:

$$f(p_i) = \frac{1}{\sqrt{2\pi}\sigma_i} \exp\left(-\frac{1}{2}\left(\frac{p_i - \hat{p}_i}{\sigma_i}\right)^2\right) \quad (3.4)$$

<sup>1</sup> Alternatively, the  $5 \times 5$  matrix can be split in a  $3 \times 3$  matrix describing the parameters in the  $(x, y)$  plane ( $a_0, \phi_0, Q/p_T$ ), and a  $2 \times 2$  matrix describing the parameters in the  $(r, z)$  plane ( $z_0, \cot\theta$ ). See also appendix A.

with  $f(p_i)$  the probability density function for measuring track parameter  $p_i$ . One multidimensional normal distribution based on one covariance matrix  $\mathbf{C}$  can describe the complete resolution distribution for a given track  $\hat{\mathbf{p}}$ :

$$f(\mathbf{p}) = \frac{1}{(2\pi)^{2/2} \sqrt{|\mathbf{C}|}} \exp\left(-\frac{1}{2}(\mathbf{p} - \hat{\mathbf{p}})^T \mathbf{C}^{-1} (\mathbf{p} - \hat{\mathbf{p}})\right) \quad (3.5)$$

A modified version of the Monte Carlo program called PRESOL [10] has been used to calculate a set of covariance matrices, for a list of  $p_T$  and  $\eta$ -values, representing the complete range of interest. A set of 14  $p_T$ -values is used, varying between 0.5 GeV and 1 TeV (0.5 GeV, 1 GeV, 1.5 GeV, 2 GeV, 3 GeV, 4 GeV, 5 GeV, 10 GeV, 20 GeV, 40 GeV, 100 GeV, 200 GeV, 500 GeV and 1 TeV). A set of 26  $|\eta|$ -values is used, homogeneously distributed between 0 and 2.5 (step size 0.1). For each pair of  $p_T$  and  $\eta$ -values one matrix has been calculated and stored. This matrix has been calculated as the weighted average<sup>2</sup> of approximately 50 matrices for different  $z_0$ , distributed according to a Gaussian profile around  $z = 0$ , to take into account the length of the interaction region along the beam axis (section 1.3). The fluctuations in the covariances for different values of  $z_0$  are mostly within 10%. The resolution calculated by PRESOL is a good approximation to the current best estimate of the inner detector performance [11]. The calculation of these matrices is described in more detail in the following section.

The covariance matrix used for the smearing is calculated via interpolation from this set of covariance matrices. The four matrices with the nearest higher and lower  $p_T$ -values and  $\eta$ -values are used in the interpolation. The interpolation is a standard two-dimensional interpolation, linear in  $p_T^{-2}$  and  $\eta$ . An interpolation linear in  $p_T^{-2}$ , instead of linear in  $p_T$ , is used, because for a given  $\eta$ -value the resolution is approximately given by (section 3.5):

$$\sigma = A \oplus \frac{B}{p_T} \quad (3.6)$$

### Smearing of primary pion track parameters

For primary pions, two uncorrelated parts, a Gaussian centre part and a Gaussian tail, can describe the resolution of each track parameter [9]. Effects like scattering at large angles and track reconstruction errors (e.g. the assignment of wrong hits to the reconstructed track) are included in the tail. Two covariance matrices are necessary to describe the complete resolution distribution. For the smearing one of the two corresponding covariance matrices is used, according to the probability that a track is in the centre part or in the tail. The Gaussian centre part is identical for muons and primary pions. The calculation of the covariance matrix for the tail is described in more detail in section 3.9.

### Smearing of electron track parameters

For electrons, the smearing is more complicated. The division in an uncorrelated Gaussian part and a Gaussian tail is probably not correct. Especially important are the tails due to bremsstrahlung energy losses. At the moment only an empirical description for the smearing of electrons is available [12].

---

<sup>2</sup> The best method is to calculate the average of the matrix coefficients. The original version of PRESOL (which produced the data in the TDR [11]) calculated the average of the sigma values. Especially for  $\eta = 0$ , where results for different  $z_0$  vary most, this method can cause the final matrix to be non-positive definite.

#### Smearing of secondary pion track parameters

Secondary pions are created in the decay of  $K_S^0$  mesons, and are especially important for B-physics studies. Because a  $K_S^0$  meson is a relatively stable particle, it can pass one or several precision layers before it decays into two pions. A consequence of this is that the covariance matrix used for the smearing can not be calculated via an interpolation based on the  $p_T$  and  $\eta$ -values. Also the radius  $r$  of the decay vertex should be taken into account. The resolution of a secondary pion will be worse than of a primary pion if precision layers are missed. An even more serious problem is that the pseudorapidity  $\eta$  is only a well-defined quantity for particles created near the interaction point. At the moment only an empirical description for the smearing of secondary pions is available [12].

### 3.4 Calculation of covariance matrices for the inner detector

#### 3.4.1 Introduction

This section describes the model implemented in PRESOL to calculate covariance matrices of the track parameter that are the input for the inner detector performance parameterisations. The detector model implemented in the program PRESOL is described in section 3.4.2. The calculation of the covariance matrix for the inner detector is described in section 3.4.3.

#### 3.4.2 Detector model

The complete TRT and precision tracker are implemented in PRESOL, including the pixel detectors, and optionally including the B-layer. All sub-detectors are modelled as continuous surfaces in a cylindrical geometry. All detector resolutions are based on full detector simulation (see section 3.2.1). The material is implemented in a simplified form. Local inhomogeneities are ignored. The agreement between the results from PRESOL and the results from full detector simulation is very good [11].

#### Magnetic field implementation

Both an ideal uniform 2 T magnetic field and a more realistic solenoid field are available. The solenoid field has an axial length of 5.3 m. The influence of material placed in the magnetic field is not taken into account (ideal solenoid). This is allowed because the iron in the hadronic calorimeter is far away.

#### TRT implementation

The TRT is implemented in a simplified form [13]. The implementation is based on so-called **superlayers**, combining several layers of straw tubes. The orientation of a superlayer does not always agree with the orientation of the straw tubes in the TRT. The TRT is modelled as a barrel part, extending to  $|z| = 74$  cm, a so-called extended barrel part, extending to  $|z| = 2.8$  m, and an end-cap part extending to  $|z| = 3.35$  m. The barrel part consists of eight cylindrical superlayers. The last part of the barrel is implemented as a disk with a resolution of  $70\ \mu\text{m}$  placed at  $z = 74$  cm. The extended barrel part is divided in three parts, each consisting of eight cylindrical superlayers. The last part has a somewhat worse resolution due to the lower straw density. The end-cap part is divided in eight discs. The resolutions are given in table 3.1. The resolutions used are slightly different from the TRT resolutions given in [14], to reproduce the results of full detector simulation.

#### SCT implementation

The SCT consists of cylindrical surfaces in the barrel and rings mounted on discs in the end-cap. The 2 mm dead area in the middle of the long strips is taken into account (see sec-

tion 2.4.2). The resolutions are given in table 3.1. The resolution of the inner ring of wheel 8 (small strips, see section 2.4.2) is equal to the outer part of the middle ring given in table 3.1.

**Table 3.1** Inner detector resolutions used in PRESOL [13].

system	position	longitudinal ( $L$ ) resolution [ $\mu\text{m}$ ]	transversal ( $T$ ) resolution [ $\mu\text{m}$ ]
pixel detector	barrel layer	87	12
	end-cap disk	78	13
SCT	barrel layer	530	15
	end-cap inner ring	396	11
	end-cap middle ring, inner part	509	14
	end-cap middle ring, outer part	605	17
	end-cap outer ring, inner part	513	15
	end-cap outer ring, outer part	588	17
TRT	barrel	-	100 (superlayer)
	barrel disk	-	70 (disk)
	extended barrel 1	-	100 (superlayer)
	extended barrel 2	-	100 (superlayer)
	extended barrel 3	-	124 (superlayer)
	end-cap	-	100 (disk)

### Multiple scattering

Multiple scattering in both the detection elements and the services is taken into account. The values of the thickness in radiation lengths ( $l$ ) implemented in PRESOL for the detection elements of the inner detector are given in table 3.2 (normal incidence). The services, like support material, material for electronics, cables, insulation and cooling pipes, implemented in PRESOL are given in table 3.3 (barrel) and table 3.4 (end-cap) (thickness for normal incidence). These services are also visible in the engineering layout of the inner detector (figure 2.7).

### The use of a beam constraint

One can optionally use a beam constraint, requiring that the track is created at (or very close to) the primary vertex. The beam constraint can be used as an extra measurement of the transverse position with a value of 0 and a Gaussian error of  $15\text{ }\mu\text{m}$  (beam radius). In this case a measurement of  $a_0$  makes sense only when the resolution of  $a_0$  without beam constraint is better than  $15\text{ }\mu\text{m}$ . This is only true if a B-layer is used and if the track has a  $p_T$  of more than  $20\text{ GeV}$  (section 3.6.2). Therefore no covariances including  $a_0$  with beam constraint are given in this chapter.



**Table 3.2** Inner detector radiation lengths used in *PRESOL* [13].

system	position	$l$ [%]
pixel detector	B-layer	2.34 (including supports)
	other barrel layer	2.68 (including supports)
	end-cap disk	1.3
SCT	barrel layer	2.28
	end-cap ring	2.2
TRT	barrel	1.43 (superlayer)
	barrel disk	1.0 (disk)
	extended barrel	2.3(superlayer)
	extended barrel half density	2.3 (superlayer)
	end-cap	2.3 (disk)

**Table 3.3** Barrel services implemented in *PRESOL* [13].

services	$r$ [mm]	$z_{min}$ [mm]	$z_{max}$ [mm]	$l$ [%]
barrel support	225	0	440	0.20
pixel services	230	440	778	2.40
pixel services	230	778	1071	0.40
TRT inner support	555	0	760	3.03
TRT inner material	585	0	400	1.43
SCT insulation	610	830	2795	4.30
end-cap TRT electronics	1040	830	3400	1.50
external services TRT + SCT	1070	760	960	2.45
external services TRT + SCT	1070	960	1680	3.70
external services TRT + SCT	1070	1680	2540	5.35
external services TRT + SCT	1070	2540	3400	6.60

**Table 3.4** End-cap services implemented in *PRESOL* [13].

services	$z$ [mm]	$r_{min}$ [mm]	$r_{max}$ [mm]	$l$ [%]
pixel disk services	440	39	110	1.00
pixel disk services	440	110	230	3.30
pixel disk services	440	230	270	1.00
SCT flange	765	270	555	2.60
TRT electronics	766	555	1070	2.75
services end-cap SCT	780	270	1070	1.50
services end-cap SCT	788	300	1070	0.92
services end-cap SCT	796	373	1070	0.92
services end-cap SCT	804	447	1070	0.92
services end-cap SCT	812	520	1070	0.92
end-cap service crack	2800	450	1030	4.30

### 3.4.3 Derivation of the covariance matrix

In this section the covariance matrix for the inner detector is derived. The covariance matrix can be calculated from the  $\chi^2$ -value for a fit of the predicted track position to the measured track position. The predicted track position can be calculated from the track equations for a charged track in the magnetic field of the inner detector. First the track equations are presented, followed by the contribution from the intrinsic detector resolution to the  $\chi^2$ -value and the contribution from the multiple scattering to the  $\chi^2$ -value. Finally the method to calculate the covariance matrix from the  $\chi^2$ -value is described.

#### Track equations

A vector  $\mathbf{h} = (t, z)$ , with  $t = r\phi$  (transverse co-ordinate), can represent the measurements of the co-ordinates at which a track crosses a detector plane. In the barrel these measurements can be predicted as a function of  $r$  and the track parameter vector  $\mathbf{p}$  (3.1). In a high-momentum approximation, and for  $|z - z_0| \gg |a_0|$ , the predicted co-ordinate vector  $\hat{\mathbf{h}} = (\hat{t}, \hat{z})$  is for a homogenous field given by (equation (B.13) in appendix B):

$$\begin{aligned}\hat{t}(r, \mathbf{p})[\text{m}] &= -a_0[\text{m}] + \phi_0 r[\text{m}] - 0.15 B[\text{T}] r^2[\text{m}^2] \frac{Q[\text{e}]}{p_T[\text{GeV}]} \\ \hat{z}(r, \mathbf{p})[\text{m}] &= z_0[\text{m}] + r \cot \theta[\text{m}]\end{aligned}\quad (3.7)$$

These expressions are also used in the end-cap where  $\hat{r}(z, \mathbf{p})$  instead of  $\hat{z}(r, \mathbf{p})$  gives the predicted position (see below). For a solenoid magnetic field along the  $z$ -axis,  $\vec{B}$  is a function of  $r$  and  $z$ :  $\vec{B} = \vec{B}(r, z)$ . In this case (3.7) should be replaced by [15]:

$$\begin{aligned}\hat{t}(r, \mathbf{p}) &= -a_0 + \phi_0 r - 0.3 \frac{Q}{p_T} I(r, \mathbf{p}) \\ \hat{z}(r, \mathbf{p}) &= z_0 + r \cot \theta\end{aligned}\quad (3.8)$$

with  $I(r, \mathbf{p})$  given by:

$$I(r, \mathbf{p}) = \int_0^r \int_0^{r'} (B_z(r'', \hat{z}(r'', \mathbf{p})) - \cot \theta B_r(r'', \hat{z}(r'', \mathbf{p}))) dr' dr'' \quad (3.9)$$

The change in  $\cot \theta$  due to  $B_r$  is neglected in these expressions.

Multiple scattering at the detector planes introduces additional parameters  $\mathbf{p}_{ms}$ , i.e. the two (fitted) deflections ( $\Delta\phi$ ,  $\Delta\cot\theta$ ) at each detection plane:

$$\mathbf{p}_{ms} = (\Delta\phi_1, \Delta\cot\theta_1, \Delta\phi_2, \Delta\cot\theta_2, \dots, \Delta\phi_n, \Delta\cot\theta_n) \quad (3.10)$$

For  $n$  detection planes,  $\mathbf{p}_{ms}$  has  $2n - 2$  (instead of  $2n$ ) terms unequal to zero, because only the multiple scattering that occurred in the material in front of the measurement influences a measurement. This means  $\Delta\phi_n = 0$  and  $\Delta\cot\theta_n = 0$ . The scattering processes in the different planes are independent from each other. The multiple scattering angles  $\mathbf{p}_{ms}$ , together with the helix-parameters  $\mathbf{p}$ , give a full description of the path of a particle through the detector. The expected co-ordinate at plane  $i$ ,  $\hat{h}_i(r_i, \mathbf{p}, \mathbf{p}_{ms})$ , is now given by:

$$\begin{aligned}\hat{t}_i(r_i, \mathbf{p}, \mathbf{p}_{ms}) &= -a_0 + \phi_0 r_i - 0.3 \frac{Q}{p_T} I(r, \mathbf{p}) + \sum_{j=1}^{i-1} \Delta\phi_j (r_i - r_j) \\ \hat{z}_i(r_i, \mathbf{p}, \mathbf{p}_{ms}) &= z_0 + \cot \theta r_i + \sum_{j=1}^{i-1} \Delta\cot \theta_j (r_i - r_j)\end{aligned}\quad (3.11)$$

The  $\chi^2$ -value for a least square fit of this prediction to the measurements can be split into a contribution from the intrinsic errors and a contribution from the multiple scattering terms:

$$\chi^2 = \chi_{in}^2 + \chi_{ms}^2 \quad (3.12)$$

#### Intrinsic error contribution

For a set of  $n$  detection planes, the intrinsic part  $\chi_{in}^2$  is given by:

$$\chi_{in}^2 = \frac{1}{2} \sum_{i=1}^n \left( \mathbf{h}_i - \hat{\mathbf{h}}_i(r_i, \mathbf{p}, \mathbf{p}_{ms}) \right)^T \mathbf{R}_{ii}^{-1} \left( \mathbf{h}_i - \hat{\mathbf{h}}_i(r_i, \mathbf{p}, \mathbf{p}_{ms}) \right) \quad (3.13)$$

The genuine error in the measurement of the position  $\mathbf{h}_i$  at which the particle crossed plane number  $i$  is given through the plane's intrinsic resolutions and included in (3.13) through the term  $\mathbf{R}_{ii}^{-1}$ . This term is the inverse covariance matrix of  $\mathbf{h}_i$ . In our case  $\mathbf{R}_{ii}$  has the following form<sup>3</sup>:

$$\mathbf{R}_{ii} = \begin{pmatrix} \sigma_{r\phi,i}^2 & 0 \\ 0 & \sigma_{z,i}^2 \end{pmatrix} \quad (3.14)$$

Both barrel and end-cap detectors do not necessarily measure  $r\phi$  and  $z$  directly, but rather a longitudinal and transverse co-ordinate. The longitudinal co-ordinate is parallel to a strip or row of pixels, the transverse co-ordinate is perpendicular to it.

For the barrel SCT, the relation between the detectors intrinsic resolutions at normal incidence ( $\sigma_L$ ,  $\sigma_T$ ) and the errors ( $\sigma_{r\phi}$ ,  $\sigma_z$ ) is given as follows:

$$\sigma_{r\phi} = \sigma_T \quad \sigma_z = \sigma_L \quad (3.15)$$

For the barrel pixel detector, this relation is given by:

$$\sigma_{r\phi} = \Omega \cdot \sigma_T \quad \sigma_z = \frac{\sigma_L}{\sin \theta + \cos \theta} \quad (3.16)$$

The term  $(\sin \theta + \cos \theta)^{-1}$  describes the pixel resolution as function of  $\theta$ . The resolution improves for increasing  $\theta$ , due to the increased cluster size. The position resolution for a cluster of adjacent pixels is better than for a single pixel. For bigger values of  $\theta$  the resolution gets worse again, because the clusters become too big and break up. For (3.16), the best resolution is at  $45^\circ$ . The factor  $\Omega$  is an  $|\eta|$  dependant correction term, varying between 1 and 0.58 [10]:

$$\begin{aligned} |\cot \theta| < 1 & \quad \Omega = 1 \\ 1 \leq |\cot \theta| < 4.2 & \quad \Omega = \sqrt[5]{\tan \theta} \\ 4.2 \leq |\cot \theta| < 5.4 & \quad \Omega = 0.63 \\ |\cot \theta| \geq 5.4 & \quad \Omega = 0.58 \end{aligned} \quad (3.17)$$

Both  $(\sin \theta + \cos \theta)^{-1}$  and  $\Omega$  are empirical terms to tune the resolution to the full simulation.

In the end-cap area  $r$  and not  $z$  is measured:  $\sigma_L = \sigma_r$ . The predicted position is actually also  $\hat{r}(z)$  with  $z$  as independent variable instead of  $\hat{z}(r)$  with  $r$  as independent variable. To be

---

<sup>3</sup> This is a diagonal matrix because the coupling of the two co-ordinates by the small stereo angle is neglected.

able to combine the barrel and end-cap in one expression, also in the end-cap  $r$  is used as independent variable. Neglecting  $z_0$ , the relation between  $r$  and  $z$  is given by:

$$z = r \cot \theta \quad (3.18)$$

This means that the error on the “measured” position  $z$  is given by:

$$\sigma_z = \sigma_r \cot \theta \quad (3.19)$$

In this case the relation between  $\sigma_{r\phi}$  and  $\sigma_z$  and the longitudinal and transversal errors are given by (both for the pixel detector and SCT):

$$\sigma_{r\phi} = \sigma_T \quad \sigma_z = \sigma_L \cot \theta \quad (3.20)$$

### Multiple scattering contribution

For a set of  $m = n - 1$  scattering planes, the multiple scattering term  $\chi_{ms}^2$  is given by:

$$\chi_{ms}^2 = \frac{1}{2} \sum_{i=1}^m \mathbf{p}_{i,ms}^T \mathbf{N}_{ii}^{-1} \mathbf{p}_{i,ms} \quad (3.21)$$

The vector  $\mathbf{p}_{i,ms}$  of the scattering angles is given by:

$$\mathbf{p}_{i,ms} = (\Delta\phi_i, \Delta\cot\theta_i) \quad (3.22)$$

The matrix  $\mathbf{N}_{ii}$  describes the rms of the scattering angle at plane  $i$ :

$$\mathbf{N}_{ii} = \begin{pmatrix} \frac{k_{i,1}^2}{p_T^2} & 0 \\ 0 & \frac{k_{i,2}^2}{p_T^2} \end{pmatrix} \quad (3.23)$$

The terms  $k_{i,1}$  and  $k_{i,2}$  [GeV] are given by:

$$k_{i,1} = 0.0136 \sqrt{L_i (1 + 0.038 \log L_i)^2 - L_{i-1} (1 + 0.038 \log L_{i-1})^2} \quad k_{i,2} = \frac{k_{i,1}}{\sin \theta} \quad (3.24)$$

The term  $L_i$  describes the total thickness in radiation lengths, summed over all planes up to the current plane  $i$ :

$$L_i = \sum_{j=1}^i l_j \quad (3.25)$$

The term  $l_i$  describes the thickness of scattering plane  $i$  in radiation lengths. Equation (3.23) and (3.24) are an extension of the formula given in [16], describing a single scattering for a track at normal incidence.

### Calculation of the covariance matrix

Equation (3.13) and (3.21) can be combined into one expression if the scattering angles at each detector plane (3.22) are also regarded as measurements and are always zero. The multiple scattering planes coming from the services are regarded as measurement planes with infinite resolution ( $\sigma = \infty$ ). The measured position at plane  $i$  is now given by:

$$\mathbf{h}_i = (t_i, z_i, 0, 0) \quad (3.26)$$

The predicted position  $\hat{\mathbf{h}}_i$  at plane  $i$  is given by:

$$\hat{\mathbf{h}}_i = (\hat{r}_i(r, \mathbf{p}, \mathbf{p}_{ms}), \hat{z}_i(r, \mathbf{p}, \mathbf{p}_{ms}), \Delta\phi_i, \Delta\cot\theta_i) \quad (3.27)$$

The total  $\chi^2$ -value is now given by:

$$\chi^2 = \frac{1}{2} \sum_{i=1}^n (\mathbf{h}_i - \hat{\mathbf{h}}_i(r_i, \mathbf{p}, \mathbf{p}_{ms}))^T \mathbf{V}_{ii}^{-1} (\mathbf{h}_i - \hat{\mathbf{h}}_i(r_i, \mathbf{p}, \mathbf{p}_{ms})) \quad (3.28)$$

The  $4 \times 4$  diagonal matrix  $\mathbf{V}_{ii}$  is given by the direct sum of the matrices  $\mathbf{R}_{ii}$  (3.14) and  $\mathbf{N}_{ii}$  (3.23):

$$\mathbf{V}_{ii} = \begin{pmatrix} \mathbf{R}_{ii} & \mathbf{0} \\ \mathbf{0} & \mathbf{N}_{ii} \end{pmatrix} \quad (3.29)$$

Having expressed the  $\chi^2$ -value in terms of  $\mathbf{V}_{ii}$ ,  $\mathbf{h}_i$  and  $\hat{\mathbf{h}}_i$  and knowing the functional dependence of  $\hat{\mathbf{h}}_i$  from the track parameters  $\mathbf{p}$  and multiple scattering parameters  $\mathbf{p}_{ms}$ , one can analytically determine the inverse covariance matrix  $\mathbf{C}^{-1}$  of  $\mathbf{p}$  and  $\mathbf{p}_{ms}$  ([17] see also [18]):

$$\frac{\partial^2 \chi^2}{\partial \tilde{p}_a \partial \tilde{p}_b} = \mathbf{C}_{ab}^{-1} = \sum_{i=1}^n \mathbf{D}_{i,a}^T \mathbf{V}_{ii}^{-1} \mathbf{D}_{i,b} \quad (3.30)$$

where:

$$\mathbf{D}_{i,a} = \frac{\partial \hat{\mathbf{h}}_i}{\partial \tilde{p}_a} \quad (3.31)$$

with  $\tilde{\mathbf{p}}$  being the combined vector  $(\mathbf{p}, \mathbf{p}_{ms})$ ; Using the expression for  $\tilde{\mathbf{h}}_i$  and  $\tilde{\mathbf{p}}$ :

$$\hat{\mathbf{h}}_i = \begin{pmatrix} -a_0 + \phi_0 r_i - 0.3 \frac{Q}{p_T} I(r, \mathbf{p}) + \sum_{j=1}^{i-1} \Delta\phi_j (r_i - r_j) \\ z_0 + \cot\theta r_i + \sum_{j=1}^{i-1} \Delta\cot\theta_j (r_i - r_j) \\ \Delta\phi_i \\ \Delta\cot\theta_i \end{pmatrix} \quad (3.32)$$

$$\tilde{\mathbf{p}} = (a_0, z_0, \phi_0, \cot\theta, Q/p_T, \Delta\phi_1, \Delta\cot\theta_1, \Delta\phi_2, \Delta\cot\theta_2, \dots, \Delta\phi_n, \Delta\cot\theta_n) \quad (3.33)$$

One finds for each plane  $i$  the complete  $(5 + 2n) \times 4$  matrix  $\mathbf{D}_i$  to be:

$$\mathbf{D}_i = \begin{pmatrix} -1 & 0 & r_i & 0 & -0.15 B_i r_i^2 & r_i - r_1 & 0 & \dots & r_i - r_{i-1} & 0 & 0 & 0 & 0 & \dots & 0 \\ 0 & 1 & 0 & r_i & 0 & 0 & r_i - r_1 & \dots & 0 & r_i - r_{i-1} & 0 & 0 & 0 & \dots & 0 \\ 0 & 0 & 0 & 0 & 0 & 0 & 0 & \dots & 0 & 0 & 1 & 0 & 0 & \dots & 0 \\ 0 & 0 & 0 & 0 & 0 & 0 & 0 & \dots & 0 & 0 & 0 & 1 & 0 & \dots & 0 \end{pmatrix} \quad (3.34)$$

The term  $B_i$  describes the value of the magnetic field at the track intersection with the detector layer. In PRESOL, the  $5 \times 5$  covariance matrices  $\mathbf{C}$  as function of the original track parameters  $\mathbf{p}$  only are calculated by numerically inverting (3.30), after substituting (3.34) into it, and taking the  $5 \times 5$  sub-matrix. Matrix (3.30) is calculated for a set of predicted positions, created according to equation (3.11). In the vector of the original track parameters  $\mathbf{p}$ , the components  $a_0$  and  $\phi_0$  are always zero.

### 3.5 The $A \oplus B$ -model

The above formulas can be simplified if a measurement predominantly depends on the first two measurement planes. This is the case for the impact parameters  $a_0$  and  $z_0$  when the B-layer is present. In the case of two detection layers, the following analytic relation gives the resolution of the impact parameters (appendix A):

$$\sigma = \frac{r_1 \sigma_2 \oplus r_2 \sigma_1}{r_2 - r_1} \oplus \frac{k_1 r_1}{p_T} = A \oplus \frac{B}{p_T} \quad (3.35)$$

The position resolution of the first detector layer at  $r = r_1$  is given by  $\sigma_1$ , the position resolution of the second detector layer at  $r = r_2$  is given by  $\sigma_2$ . The term  $k_1 p_T^{-1}$  describes the rms of the multiple scattering angle at the first plane (3.24).

This form can be shown to be an asymptotic solution at very high and very low  $p_T$  to the other covariances, which are derived from (3.30) [19]. Hence, the following approximations can be written<sup>4</sup>:

$$\text{cov}(p_a) = A_{aa}^2 + \frac{B_{aa}^2}{p_T^2} \quad \text{cov}(p_a, p_b) = A_{ab}^2 + \frac{B_{ab}^2}{p_T^2} \quad (3.36)$$

The indices  $a$  and  $b$  indicate the track parameters (3.1). The symmetric  $5 \times 5$  matrix  $\mathbf{A}$  represents the intrinsic errors on the track parameters and  $\mathbf{B}$  represents the multiple scattering errors. Both  $\mathbf{A}$  and  $\mathbf{B}$  depend on  $|\eta|$  but not on  $p_T$ .

The expressions for  $A$  and  $B$ , given in (3.35), are only valid for the impact parameters  $a_0$  and  $z_0$ . For a fixed value of  $|\eta|$ , the matrices  $\mathbf{A}$  and  $\mathbf{B}$  can be determined via one measurement at low and one at high  $p_T$ . An arbitrary but useful choice is  $p_T = 1$  GeV for the low- $p_T$  measurement and  $p_T = 1$  TeV for the high- $p_T$  measurement. At  $p_T = 1$  TeV, the influence of the  $B$  term is negligible and  $\text{cov}(p_a, p_b) = A_{ab}^2$ .

## 3.6 Resolutions and correlations for the inner detector

### 3.6.1 Introduction

In this section the resolutions and correlations of all track parameters for muons are discussed. The resolutions as functions of  $\eta$  and  $p_T$  and the correlations are presented. The data points calculated with PRESOL for  $|\eta| = 0$  and different values of  $p_T$  are compared with the  $A \oplus B$ -model. The inverse momentum resolution calculated with PRESOL and implemented in the new ATLFast version (version 2.0) has been compared with the inverse momentum resolution implemented in the original ATLFast version (version 1.0).

### 3.6.2 Transverse impact parameter resolution

The resolution of the transverse impact parameter  $a_0$  as function of  $p_T$  is given in figure 3.4 ( $|\eta| = 0$ , ideal field, with and without the B-layer<sup>5</sup>). The points are calculated with PRESOL. The lines are a fit according to the  $A \oplus B$ -model (also in the figures for the other track parameters). With the B-layer, the resolution is significantly better, especially for  $p_T < 10$  GeV.

<sup>4</sup> In the inner detector TDR [11] an incorrect relation is given for the correlation terms:  $\rho_{ab} = A_{ab}^2 + B_{ab}^2 / p_T^2$ . The numerical values given in table 4-3 in [11] are not valid.

<sup>5</sup> It is not clear whether the B-layer will always be present during ATLAS running, especially at high luminosity.

With the B-layer, the  $A \oplus B$ -model describes the data very well across the complete  $p_T$ -range. Without the B-layer, rather big discrepancies of about 20% occur for intermediate  $p_T$ -values ( $1 < p_T < 10$  GeV).

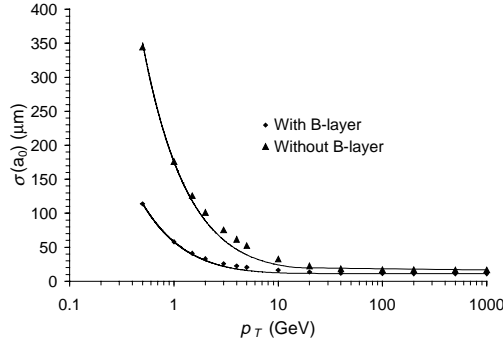


**Figure 3.4**  $\sigma(a_0)$  versus  $p_T$  for  $|\eta| = 0$ .

The impact parameter resolution  $\sigma(a_0)$  as function of  $|\eta|$  for  $p_T = 1$  TeV and  $p_T = 0.5$  GeV is given in figure 3.5 and figure 3.6. The most important contribution to the resolution comes from the first detector layer<sup>6</sup>. The resolution is nearly constant across the  $|\eta|$  coverage of the first detector layer for high- $p_T$  tracks. Outside this range the error increases sharply. This behaviour can be seen in figure 3.5 (with and without the B-layer<sup>7</sup>). The resolution even improves slightly with increasing  $|\eta|$ , due to increasing cluster size. For  $|\eta| < 2$ , the model used for the magnetic field has almost no influence on the results. The degradation without the B-layer for  $|\eta| > 2$  however strongly depends on the model used for the magnetic field.

For low- $p_T$  tracks the resolution is almost completely determined by the multiple scattering term and increases with  $|\eta|$  (more material). Without the B-layer, the resolution improves again at  $|\eta| = 2$  because the end of the coverage of the first pixel barrel layer is reached and the first measurement is now a pixel disk. This is traversed at a more favourable angle than the first barrel layer (see also figure 2.7). It therefore represents less material resulting in less multiple scattering at the first detection layer<sup>8</sup>.

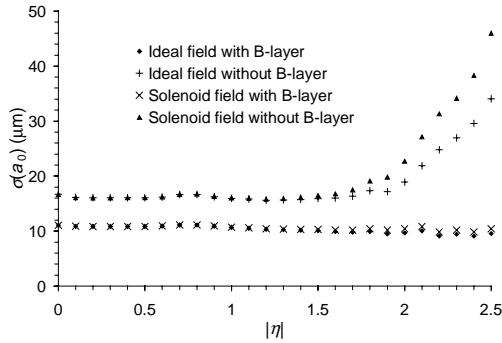


**Figure 3.5**  $\sigma(a_0)$  versus  $|\eta|$  for  $p_T = 1$  TeV.

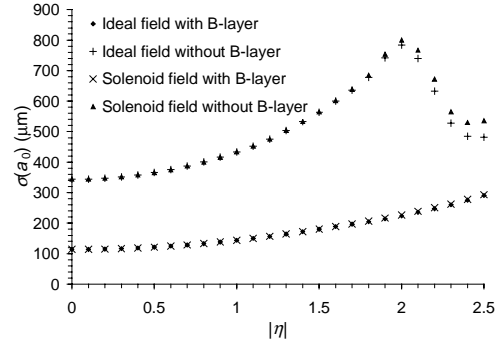


**Figure 3.6**  $\sigma(a_0)$  versus  $|\eta|$  for  $p_T = 0.5$  GeV.

<sup>6</sup> This follows directly from equation (3.35), since  $r_2 > r_1$

<sup>7</sup> The B-layer extends up to  $|\eta| = 2.5$ , the first barrel pixel layer only extends up to  $|\eta| = 2$ .

<sup>8</sup> Only the multiple scattering at the first measurement layer influences the resolution of the impact parameters.

### 3.6.3 Longitudinal impact parameter resolution

In figure 3.7  $\sigma(z_0)$  is given as function of  $p_T$  (with and without the B-layer,  $|\eta| = 0$ ). The beam constraint and magnetic field do not influence  $\sigma(z_0)$  because the track parameters in the  $(x, y)$  plane and the  $(r, z)$  plane are uncorrelated. With the B-layer, the resolution is significantly better over the complete  $p_T$ -range. The  $A \oplus B$ -model describes the data very well across the complete  $p_T$ -range, apart from the point at 0.5 GeV.

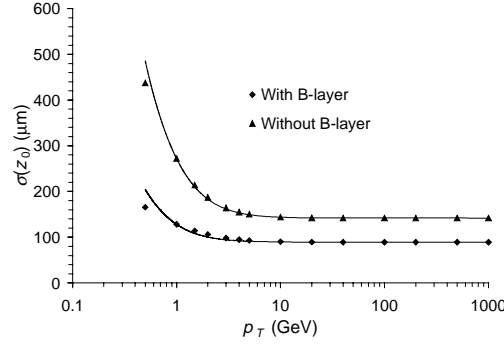


**Figure 3.7**  $\sigma(z_0)$  versus  $p_T$  for  $|\eta| = 0$ .

In figure 3.8 and figure 3.9,  $\sigma(z_0)$  is given as function of  $|\eta|$  for  $p_T = 1$  TeV and 0.5 GeV respectively. For  $p_T = 1$  TeV,  $\sigma(z_0)$  is mainly determined by the intrinsic resolution of the first two detector layers and should be approximately constant across the complete  $|\eta|$  range covered by these layers ( $|\eta| = 2.5$  with the B-layer,  $|\eta| = 2$  without the B-layer). In fact the resolution improves slightly at  $|\eta| \approx 1$ , due to the increased cluster sizes. For  $p_T = 0.5$  GeV, the multiple scattering term dominates the resolution. In this case, the behaviour is similar to that of the transverse impact parameter. The resolution in the longitudinal direction is significantly worse than in the transverse direction due to the poorer  $z$  resolution of the B-layer and pixel detectors.

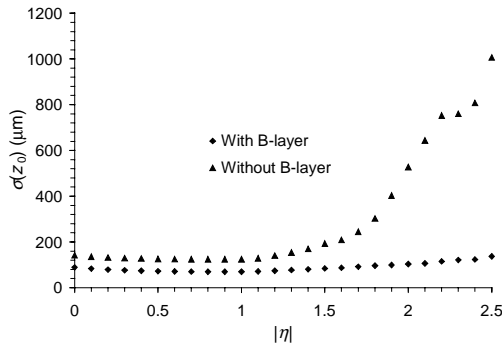


**Figure 3.8**  $\sigma(z_0)$  versus  $|\eta|$  for  $p_T = 1$  TeV.

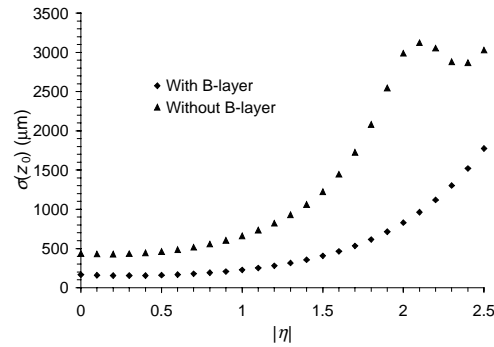


**Figure 3.9**  $\sigma(z_0)$  versus  $|\eta|$  for  $p_T = 0.5$  GeV.

### 3.6.4 Azimuthal resolution

In figure 3.10 and figure 3.11,  $\sigma(\phi_0)$  is given as function of  $p_T$  ( $\eta = 0$ , ideal field, with and without the B-layer), without and with beam constraint. Without beam constraint, the  $A \oplus B$ -model describes the data rather well. With beam constraint, it fails for intermediate  $p_T$ -values



( $1 < p_T < 10$  GeV) and low  $p_T$ -values ( $p_T < 1$  GeV)<sup>9</sup>. For  $|\eta| = 0$ , the addition of a B-layer has almost no influence on the resolution, except for  $p_T < 1$  GeV.

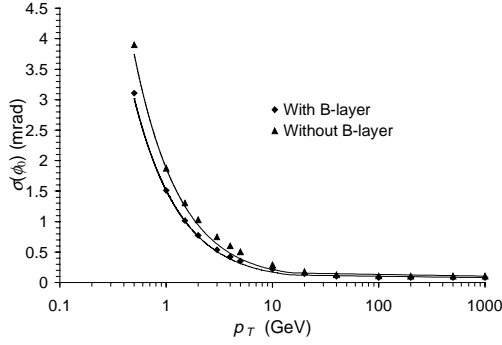


**Figure 3.10**  $\sigma(\phi_0)$  versus  $p_T$  for  $|\eta| = 0$ , no beam constraint.

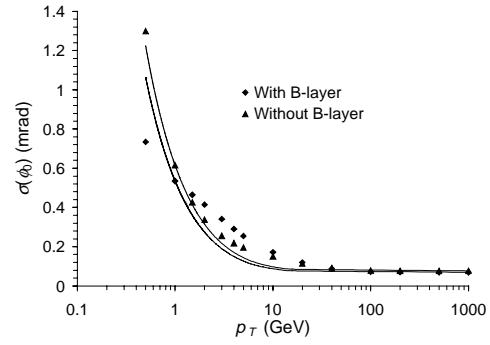


**Figure 3.11**  $\sigma(\phi_0)$  versus  $p_T$  for  $|\eta| = 0$ , beam constraint.

The azimuthal resolution  $\sigma(\phi_0)$  as function of  $|\eta|$  is given in figure 3.12 and figure 3.13 for  $p_T = 1$  TeV and  $p_T = 0.5$  GeV (no beam constraint). With the B-layer, the resolution for  $p_T = 1$  TeV is fairly constant in  $|\eta|$  and independent of the model for the magnetic field. Without the B-layer,  $\sigma(\phi_0)$  increases sharply beyond  $|\eta| = 2$ . The magnetic field strongly influences this degradation. The behaviour of  $\sigma(\phi_0)$  as function of  $|\eta|$  for  $p_T = 0.5$  GeV is similar to the behaviour of the impact parameter resolutions.

The corresponding plots with beam constraint are given in figure 3.14 and figure 3.15. The behaviour is similar to the behaviour without beam constraint. For  $p_T = 0.5$  GeV without B-layer however, there is no improvement of the resolution at  $|\eta| = 2$ .

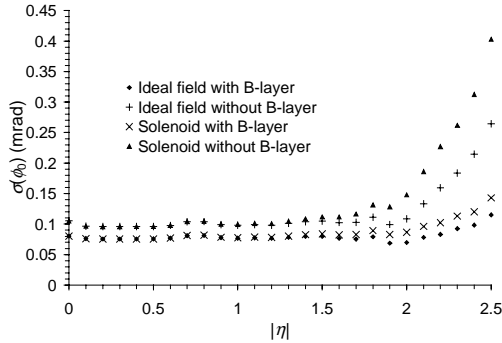


**Figure 3.12**  $\sigma(\phi_0)$  versus  $|\eta|$  for  $p_T = 1$  TeV, no beam constraint.

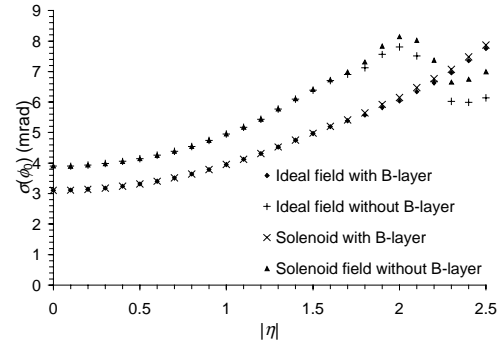


**Figure 3.13**  $\sigma(\phi_0)$  versus  $|\eta|$  for  $p_T = 0.5$  GeV, no beam constraint.

<sup>9</sup> The  $A \oplus B$ -model will match at low  $p_T$ , if the point at 0.5 GeV instead of 1 GeV is used for determining parameter  $B$ . In this case however the discrepancy at intermediate  $p_T$ -values will be even bigger.

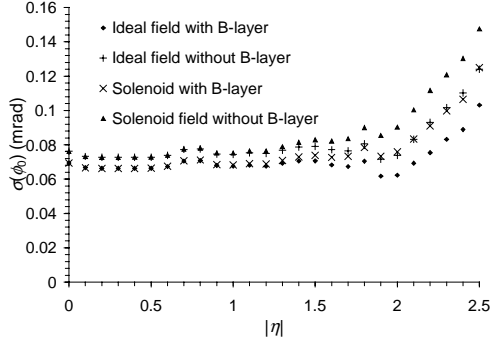


**Figure 3.14**  $\sigma(\phi_0)$  versus  $|\eta|$  for  $p_T = 1$  TeV, beam constraint.

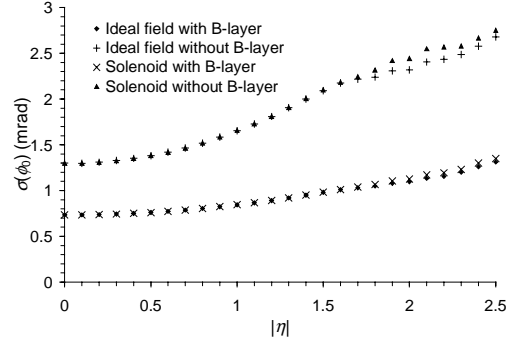


**Figure 3.15**  $\sigma(\phi_0)$  versus  $|\eta|$  for  $p_T = 0.5$  GeV, beam constraint.

### 3.6.5 Polar angle resolution

The polar angle resolution  $\sigma(\cot\theta)$  versus  $p_T$  is given in figure 3.16 ( $|\eta| = 0$ , with and without B-layer). The  $A \oplus B$ -model describes the data very well across the complete  $p_T$  range.  $\sigma(\cot\theta)$  is less sensitive than  $\sigma(z_0)$  to the removal of the B-layer.

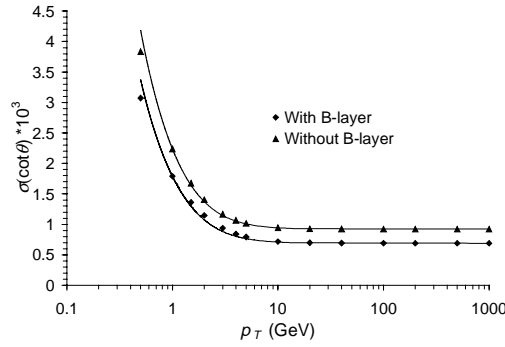


**Figure 3.16**  $\sigma(\cot\theta)$  versus  $p_T$  for  $|\eta| = 0$ .

The resolution  $\sigma(\cot\theta)$  versus  $|\eta|$  is given in figure 3.17 and figure 3.18, for  $p_T = 1$  TeV and  $p_T = 0.5$  GeV. The resolution is almost constant in the barrel area, it increases in the end-cap area. This behaviour can be explained from equation (3.15) and (3.20). These equations show that the  $z$ -resolution of the SCT is independent of  $\theta$  in the barrel area and scales with  $\cot\theta$  in the end-cap area.

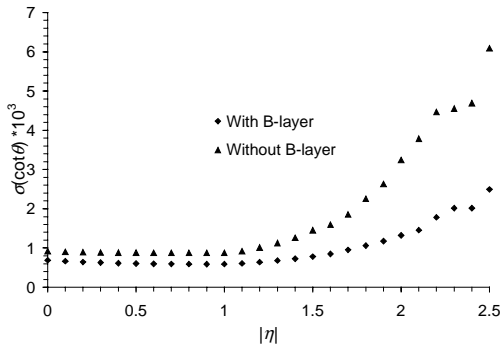


**Figure 3.17**  $\sigma(\cot\theta)$  versus  $|\eta|$  for  $p_T = 1$  TeV.

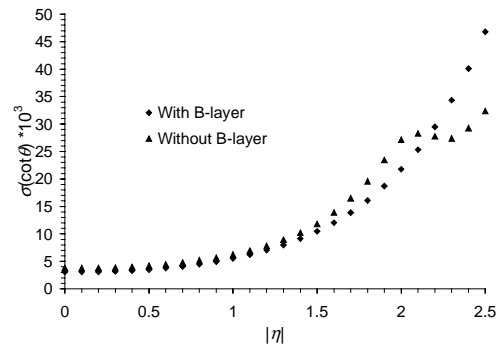


**Figure 3.18**  $\sigma(\cot\theta)$  versus  $|\eta|$  for  $p_T = 0.5$  GeV.

### 3.6.6 Inverse transverse momentum resolution

The inverse transverse momentum resolution  $\sigma(Q/p_T)$  versus  $p_T$  is shown in figure 3.19 and figure 3.20 ( $|\eta| = 0$ , ideal field, with and without the B-layer), without and with beam constraint. The  $A \oplus B$ -model matches the data well, except for  $p_T < 1$  GeV. For  $|\eta| = 0$ , the addition of a B-layer has no influence on the inverse transverse momentum resolution, over the complete  $p_T$  range.

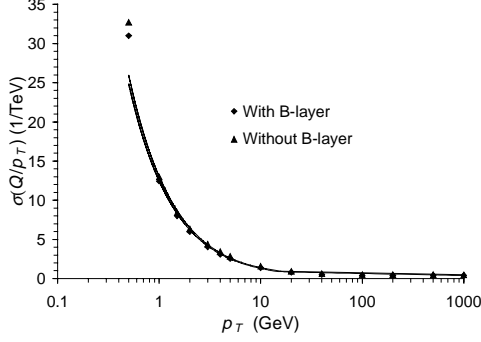


**Figure 3.19**  $\sigma(Q/p_T)$  versus  $p_T$  for  $|\eta| = 0$ , no beam constraint.

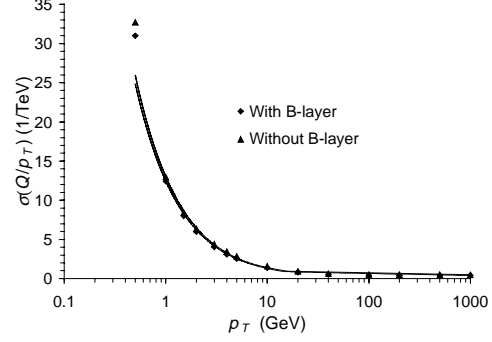


**Figure 3.20**  $\sigma(Q/p_T)$  versus  $p_T$  for  $|\eta| = 0$ , beam constraint.

The resolution  $\sigma(Q/p_T)$  versus  $|\eta|$  is given in figure 3.21 and figure 3.22 ( $p_T = 1$  TeV and  $p_T = 0.5$  GeV, no beam constraint). For  $p_T = 1$  TeV, the resolution degrades sharply above  $|\eta| = 2$ . The B-layer has almost no influence on the resolution in the central part, but beyond  $|\eta| = 2$  it helps significantly. Also the field has an important influence above  $|\eta| = 2$ . For  $p_T = 0.5$  GeV, the results are almost independent of the use of the B-layer. The magnetic field has some influence above  $|\eta| = 2$ .

The corresponding plots with beam constraint are given in figure 3.23 and figure 3.24. Above  $|\eta| = 2$ , the use of a beam constraint significantly helps to improve the resolution for  $p_T = 1$  TeV.

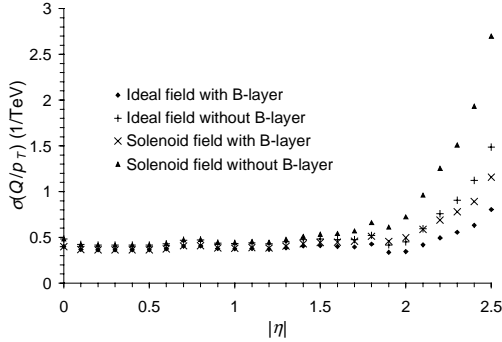


**Figure 3.21**  $\sigma(Q/p_T)$  versus  $|\eta|$  for  $p_T = 1$  TeV, no beam constraint.

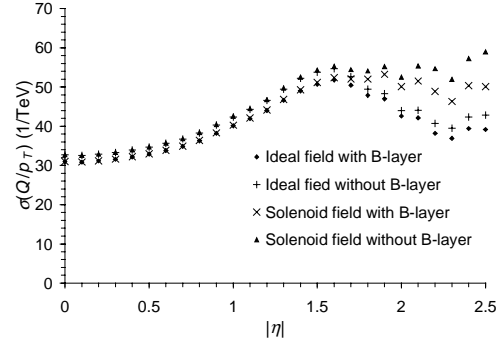


**Figure 3.22**  $\sigma(Q/p_T)$  versus  $|\eta|$  for  $p_T = 0.5$  GeV, no beam constraint.

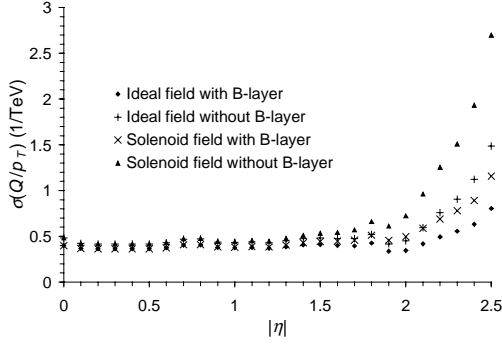


**Figure 3.21**  $\sigma(Q/p_T)$  versus  $|\eta|$  for  $p_T = 1$  TeV, **Figure 3.22**  $\sigma(Q/p_T)$  versus  $|\eta|$  for  $p_T = 0.5$  GeV, no beam constraint.

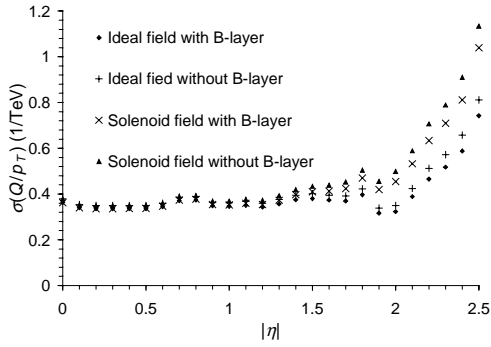
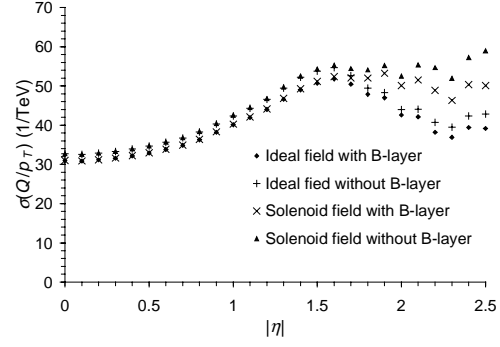
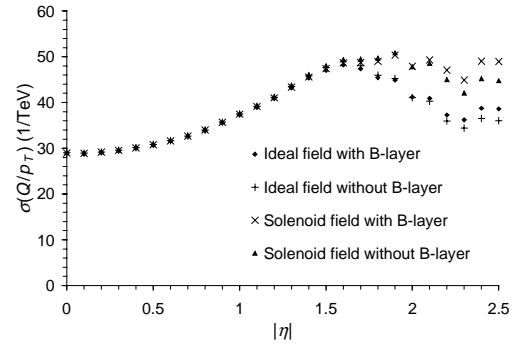


**Figure 3.23**  $\sigma(Q/p_T)$  versus  $|\eta|$  for  $p_T = 1$  TeV, **Figure 3.24**  $\sigma(Q/p_T)$  versus  $|\eta|$  for  $p_T = 0.5$  GeV, beam constraint.



### Comparison with the old parameterisation

I have compared the inverse momentum resolution for muons (B-layer, no vertex constraint and homogenous field), calculated with PRESOL, with the parameterisation of the inner detector momentum resolution, originally implemented in ATLFast. In the original ATLFast implementation, the inner detector momentum resolution as function of  $p_T$  and  $|\eta|$  is given by [2]:

$$\frac{\sigma(p_T)}{p_T} = (0.0005 p_T \oplus 0.012) \left( 1 + \frac{|\eta|^{10}}{7000} \right) \quad (3.37)$$

The momentum resolution  $\sigma(p_T)$  can be converted to the inverse momentum resolution  $\sigma(Q/p_T)$  via the following relation:

$$y = f(x_1, x_2, \dots) \Rightarrow \sigma_y = \sqrt{\sum_i \left( \frac{\partial f}{\partial x_i} \right)^2 \sigma_{x_i}^2} \quad (3.38)$$

The inverse momentum resolution  $\sigma(Q/p_T)$  is now given by:

$$\sigma(Q/p_T) = \frac{\sigma(p_T)}{p_T^2} = \left( 0.0005 \oplus \frac{0.012}{p_T} \right) \left( 1 + \frac{|\eta|^{10}}{7000} \right) \quad (3.39)$$

This expression is an extended version of the  $A \oplus B$ -model, described in section 3.5. With this extension the resolution can be calculated both as function of  $p_T$  and as function of  $|\eta|$ . A  $|\eta|$  dependent multiplication factor empirically includes the influence of  $|\eta|$ .

The inverse momentum resolution against  $|\eta|$  for  $p_T = 1$  TeV is shown in figure 3.25. The corresponding plot for  $p_T = 1$  GeV is shown in figure 3.26. The inverse momentum resolution against  $p_T$  for  $|\eta| = 0.2$  is shown in figure 3.27. The corresponding plot for  $|\eta| = 2.5$  is shown in figure 3.28. From the figures it can be concluded that for the chosen values of  $|\eta|$ , the old parameterisation correctly describes the inverse momentum resolution as function of  $p_T$ . The description of the inverse momentum resolution as function of  $|\eta|$  however, is completely wrong.

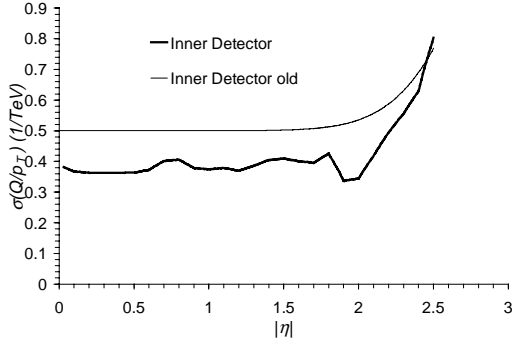


**Figure 3.25**  $\sigma(Q/p_T)$  versus  $|\eta|$ ,  $p_T = 1$  TeV.

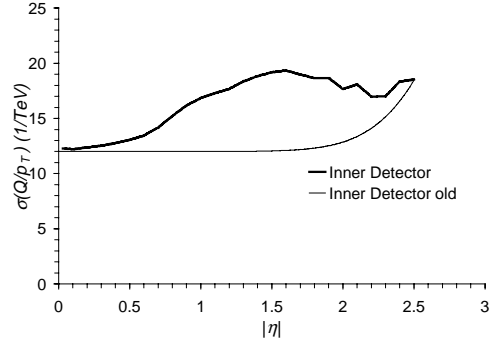


**Figure 3.26**  $\sigma(Q/p_T)$  versus  $|\eta|$ ,  $p_T = 1$  GeV.

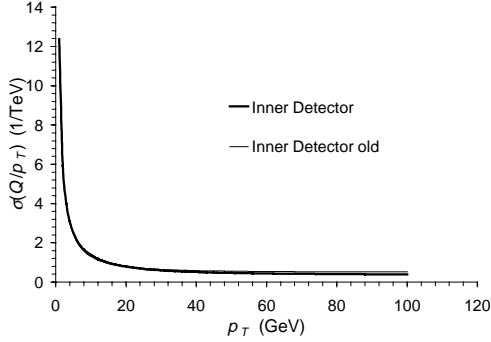


**Figure 3.27**  $\sigma(Q/p_T)$  versus  $p_T$ ,  $|\eta| = 0.2$ .

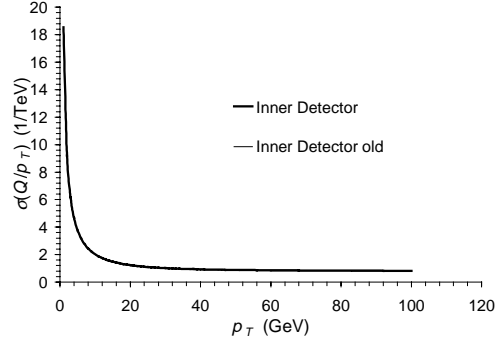


**Figure 3.28**  $\sigma(Q/p_T)$  versus  $p_T$ ,  $|\eta| = 2.5$ .

#### 3.6.7 Correlations

The covariances  $\text{cov}(a_0, \phi_0)$ ,  $\text{cov}(a_0, Q/p_T)$ ,  $\text{cov}(z_0, \cot\theta)$ ,  $\text{cov}(\phi_0, Q/p_T)$  and the corresponding normalised correlations  $\rho$ , are given as function of  $p_T$  in figure 3.29 to figure 3.38. For most covariances, the  $A \oplus B$ -model matches the data very well, except for  $p_T < 1$  GeV. In the case of beam constraint measurements of  $\text{cov}(\phi_0, Q/p_T)$ , the  $A \oplus B$ -model describes the data less well. Using the B-layer always significantly reduces the magnitude of the correlation coefficients.

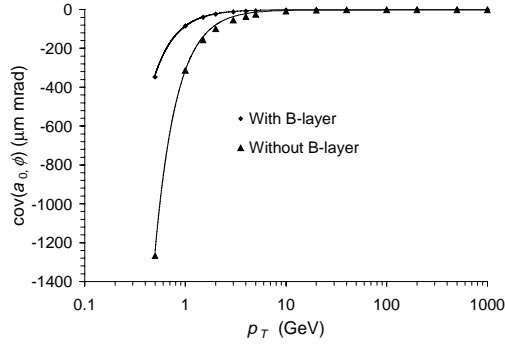


**Figure 3.29**  $\text{cov}(a_0, \phi_0)$  versus  $p_T$  for  $|\eta| = 0$ .

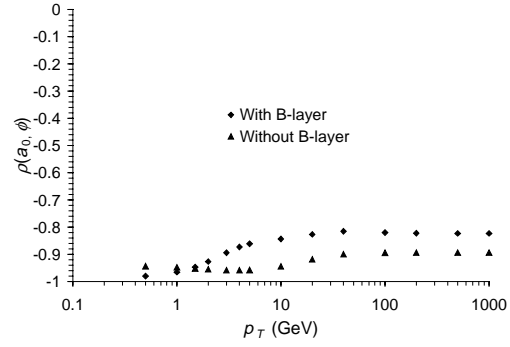


**Figure 3.30**  $\rho(a_0, \phi_0)$  versus  $p_T$  for  $|\eta| = 0$ .

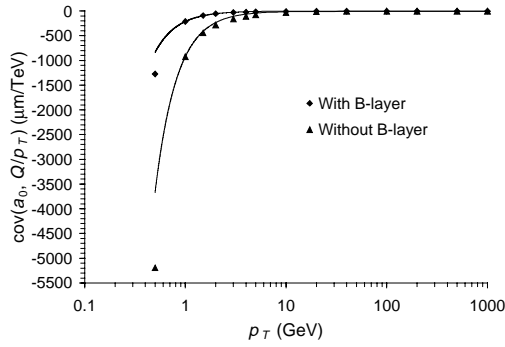


**Figure 3.31**  $\text{cov}(a_0, Q/p_T)$  versus  $p_T$  for  $|\eta| = 0$ .

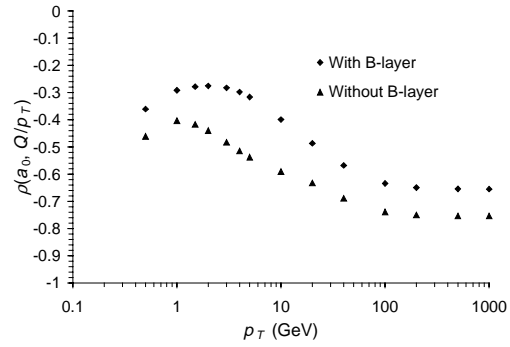


**Figure 3.32**  $\rho(a_0, Q/p_T)$  versus  $p_T$  for  $|\eta| = 0$ .

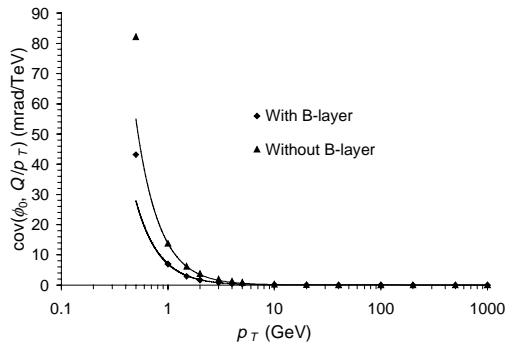


**Figure 3.33**  $\text{cov}(\phi_0, Q/p_T)$  versus  $p_T$  for  $|\eta| = 0$ , no beam constraint.

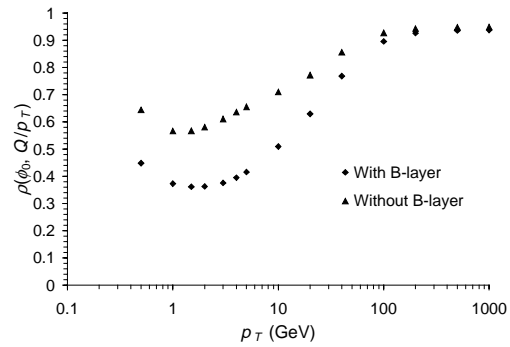


**Figure 3.34**  $\rho(\phi_0, Q/p_T)$  versus  $p_T$  for  $|\eta| = 0$ , no beam constraint.

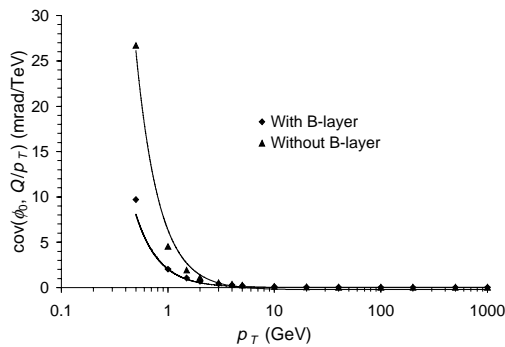


**Figure 3.35**  $\text{cov}(\phi_0, Q/p_T)$  versus  $p_T$  for  $|\eta| = 0$ , beam constraint.

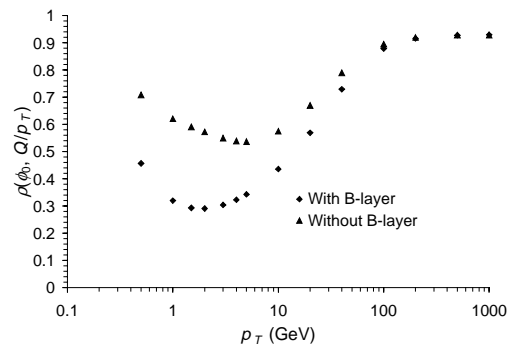


**Figure 3.36**  $\rho(\phi_0, Q/p_T)$  versus  $p_T$  for  $|\eta| = 0$ , beam constraint.

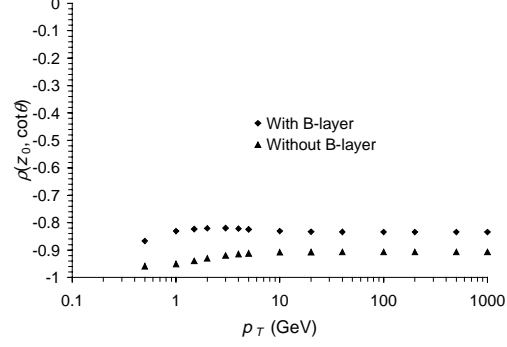
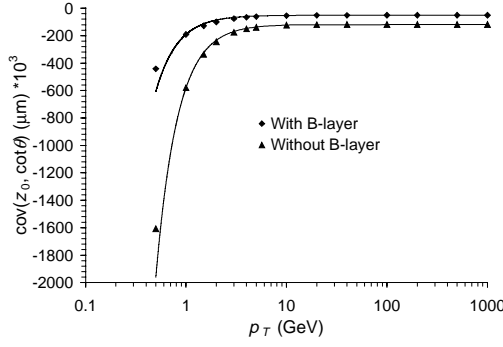


**Figure 3.37**  $\text{cov}(z_0, \cot\theta)$  versus  $p_T$  for  $|\eta| = 0$ . **Figure 3.38**  $\rho(z_0, \cot\theta)$  versus  $p_T$  for  $|\eta| = 0$ .

### 3.6.8 Conclusions

From the above data it can be concluded that the  $A \oplus B$ -model does not always match the data across the complete  $p_T$ -range for a fixed value of  $|\eta|$ . An extended version of the  $A \oplus B$ -model to calculate the resolution both as function of  $p_T$  and  $|\eta|$ , with the  $|\eta|$  dependence of the resolution included by a  $|\eta|$  dependent multiplication factor, completely fails (figure 3.25 and figure 3.26). Since all elements of the covariance matrix vary smoothly with  $|\eta|$  and  $p_T$ , a better strategy is to determine them by interpolating between matrices calculated at selected  $|\eta|$  and  $p_T$ -values. The  $A \oplus B$ -model is then only used for the interpolation. The amount of data needed to describe all track parameter resolutions and tails for the inner detector for all particle types is about 150 kB. Keeping this constantly in memory is not a problem for computing platforms typically used in high energy physics. This method is actually used in the current ATLFAST implementation.

The influence of the non-uniformity of the magnetic field is significant for the track parameters in the  $(x, y)$  plane at high  $|\eta|$  (above  $|\eta| \sim 1.5$  or  $\sim 2$ , depending on which parameter is being considered). The use of a solenoid field description will give more realistic results, which will be important for some physics studies.

The addition of the B-layer has a significant influence on the resolution of the impact parameter, over the complete studied  $|\eta|$  and  $p_T$ -range. It also significantly improves the resolution of the other parameters ( $\phi_0, \cot\theta, Q/p_T$ ) in the region  $|\eta| > 2$ , at least for high- $p_T$  tracks. For low- $p_T$  tracks, it can decrease the resolution in this area due to the increased multiple scattering. The usage of a B-layer always significantly reduces the correlation between the errors, especially for tracks with  $p_T < 100$  GeV.

## 3.7 Combined system inverse momentum resolution

### 3.7.1 Calculation of the muon spectrometer inverse momentum resolution

In ATLFAST two parameterisations of the muon system are implemented to calculate the stand-alone momentum resolution for a given muon track with momentum  $p_T$ , azimuth  $\phi$  and pseudorapidity  $\eta$ . The first implementation is an approximation, based on the  $A \oplus B$ -model [20]. The intrinsic detector resolutions are included in parameter A. The contributions from multiple scattering are included in parameter B. The parameters A and B as function of pseudorapidity  $|\eta|$  and azimuth  $\phi$  are stored in a two-dimensional table. The influence of energy loss fluctuations in the calorimeter is taken into account by the addition of an extra contribution to the resolution. An empirical relation is used to calculate this contribution as function of  $|\eta|$  and  $p_T$  of the incoming muon [21].

The method used by the second implementation is in principle similar to the method used by the program PRESOL for the inner detector, described in section 3.4.3. The trajectory of the muon through the detector is calculated. The magnetic deflection at each measurement plane traversed is calculated. Multiple scattering is taken into account by computing, for every measurement plane, a deviation, which is a linear combination of the scattering angles imparted to the muon by the material planes located in front of the current measurement plane. An estimation for the  $\chi^2$ -value is calculated from the calculated deflection values, taking into account the measurement errors and the r.m.s. multiple scattering angles. The inverse momentum resolution can now be calculated via numerical matrix inversion [22]. Effects as multiple scattering tails and track recognition errors (e.g. the assignment of wrong hits to the reconstructed track) are neglected. The implemented algorithm is described in more detail in the muon spectrometer TDR [23]. Also here the influence of energy loss fluctuations in the calorimeter is included by the addition of an extra term, based on an empirical relation. A database of the layout of the muon detector and a field map describing the toroidal magnetic field is used. This map gives for each position  $(x, y, z)$  the corresponding value of the magnetic field  $(B_x, B_y, B_z)$ . The magnetic field map is based on a numerical calculation, based on a finite element method [23]. The fringe field of the solenoid and the effect of the material placed in the magnetic field (iron in the hadronic calorimeter) are neglected. The layout database describes the complete muon spectrometer. All precision and trigger chamber dimensions and shapes, including the cut-outs for detector supports, are included. The material distribution is modelled in a simplified fashion. A number of ‘material’ planes, either parallel or perpendicular to the beam axis, is defined with an aluminium-equivalent thickness which reflects the number of radiation lengths in the actual muon chamber or magnet structural element. The momentum resolution is in excellent agreement with the momentum resolution found with a full detector simulation plus reconstruction algorithm of the muon tracks [23]. All results described in this chapter of the stand-alone muon system and the combined system are based on the second implementation.

### 3.7.2 Inverse momentum resolution for the muon spectrometer

#### Inverse momentum resolution in the $(\eta, \phi)$ plane

In figure 3.39 the inverse momentum resolution  $\sigma(Q/p_T)$  in the  $(\eta, \phi)$  plane is given for  $p_T = 1$  TeV, based on  $251 \times 100$  points, homogeneously distributed between 0 and 2.5 ( $|\eta|$ ) and  $-\pi$  and  $\pi$  ( $\phi$ ). The same plot for  $p_T = 30$  GeV is given in figure 3.40. The discontinuities in the  $(\eta, \phi)$  plane are due to the presence of support structures of the detector and toroid magnet. No measurement is available for  $|\eta| < 0.03$  over the full azimuth, because of a 30 cm gap in the chamber coverage to provide space for cables and services of the inner detector, the central solenoid and the calorimeters [23]. This gap is clearly visible, especially for  $p_T = 1$  TeV. Because a muon chamber is divided in two parts, each muon detector has a dead area in the middle. The peaks due to these dead areas at  $\phi = -\frac{1}{2}\pi$ ,  $\phi = 0$  and  $\phi = \frac{1}{2}\pi$  have been removed in figure 3.39 and figure 3.40.



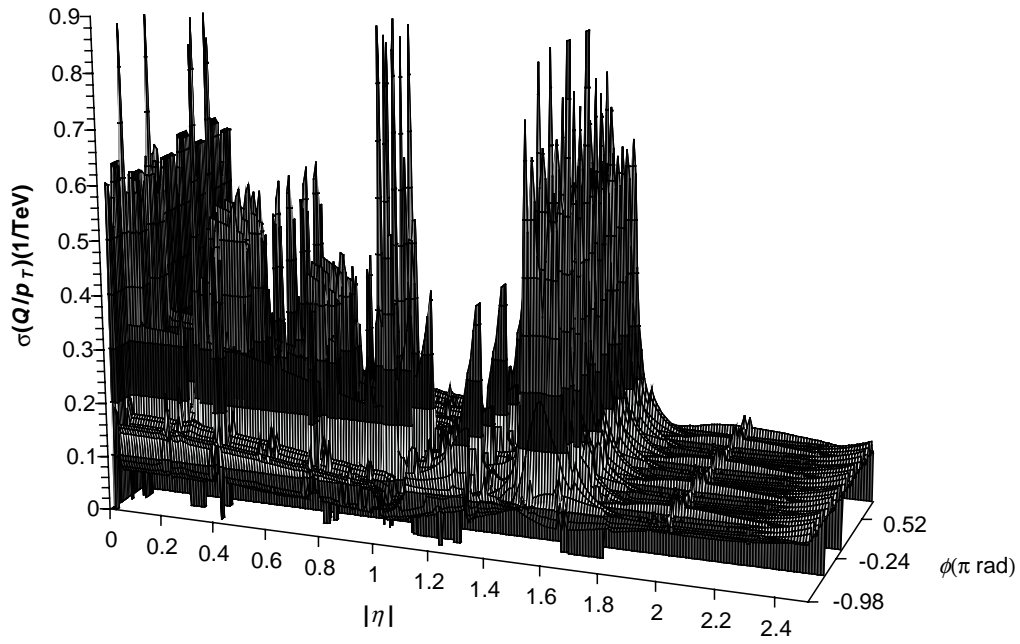


Figure 3.39  $\sigma(Q/p_T)$  muon spectrometer versus  $\eta$  and  $\phi$  ( $p_T = 1 \text{ TeV}$ ).

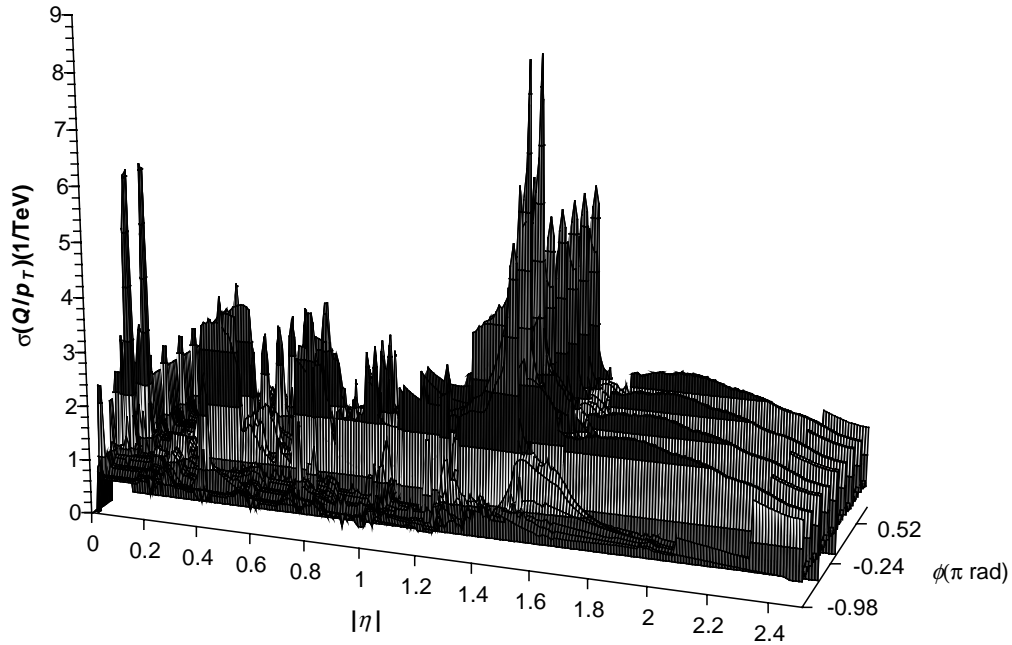


Figure 3.40  $\sigma(Q/p_T)$  muon spectrometer versus  $\eta$  and  $\phi$  ( $p_T = 30 \text{ GeV}$ ).

### Inverse momentum resolution versus $\phi$

The inverse momentum resolution  $\sigma(Q/p_T)$  as function of  $\phi$  (averaged over  $\eta$ ) is given in figure 3.41 ( $p_T = 1$  TeV) and figure 3.42 ( $p_T = 30$  GeV). The dead areas in the middle of the big muon chambers correspond to the peaks at  $\phi = \frac{1}{2}\pi$ ,  $\phi = 0$ ,  $\phi = -\frac{1}{2}\pi$ ,  $\phi = \frac{1}{4}\pi$ ,  $\phi = \frac{3}{4}\pi$ ,  $\phi = -\frac{1}{4}\pi$  and  $\phi = -\frac{3}{4}\pi$ . Due to the used set of data points the peaks at  $\phi = \frac{1}{2}\pi$ ,  $\phi = 0$  and  $\phi = -\frac{1}{2}\pi$  are larger than the other peaks. The dead area at  $\phi = \pi$  is not clearly visible. Also this is due to the used set of data points. The dead areas in the middle of the small muon chambers correspond to the peaks at  $\phi = \frac{1}{8}\pi$ ,  $\phi = \frac{3}{8}\pi$ ,  $\phi = \frac{5}{8}\pi$ ,  $\phi = \frac{7}{8}\pi$ ,  $\phi = -\frac{1}{8}\pi$ ,  $\phi = -\frac{3}{8}\pi$ ,  $\phi = -\frac{5}{8}\pi$  and  $\phi = -\frac{7}{8}\pi$ . In a dead area the relative momentum resolution is parameterised as 100% ( $\sigma(p_T) = p_T$ ). The absolute value of the inverse momentum resolution is meaningless in a dead area.

The resolution between 0 and  $-\frac{1}{2}\pi$  and between  $-\frac{1}{2}\pi$  and  $-\pi$  is worse than the resolution between 0 and  $\frac{1}{2}\pi$  and between  $\frac{1}{2}\pi$  and  $\pi$ . This is due to the presence of supporting structures in these areas. In these areas the coils with small chambers have only two detection layers [23].

From the figures it follows that the best resolution is always achieved at the edge of the muon chambers, where measurements in both triplets of small and large chambers are available.

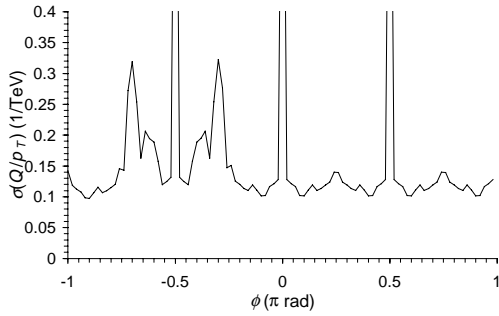


**Figure 3.41**  $\sigma(Q/p_T)$  muon spectrometer versus  $\phi$ , averaged over  $\eta$  ( $p_T = 1$  TeV).

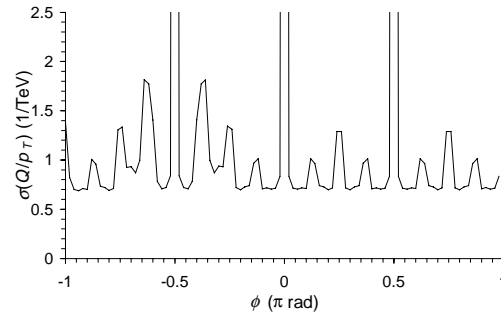


**Figure 3.42**  $\sigma(Q/p_T)$  muon spectrometer versus  $\phi$ , averaged over  $\eta$  ( $p_T = 30$  GeV).

### Inverse momentum resolution versus $|\eta|$

The inverse momentum resolution  $\sigma(Q/p_T)$  as function of  $|\eta|$  (averaged over  $\phi$ ) is given in figure 3.43 and figure 3.44. The peaks observed at  $|\eta| = 0.4$  and  $|\eta| = 0.8$  correspond to muons traversing the radial reinforcements of the barrel coils (“coil ribs”) thereby missing the middle chamber [23]. A measurement using the inner and outer chamber only is still possible, although with degraded accuracy. The large peak at  $|\eta| = 1.2$  reflects the fact that the last innermost small barrel chamber provides incomplete azimuthal coverage because of a space conflict with the innermost large end-cap chamber [23]. This causes a gap in three-chamber coverage over part of the azimuth. Several additional smaller “bumps” are also visible. These correspond to  $\eta$ -values where the resolution is dominated by multiple scattering in the “voussoirs” or “struts” of the barrel toroid [23]. The “voussoirs” provide an inner azimuthal connection between the barrel toroid coils. The “struts” provide an outer azimuthal connection between the barrel toroid coils [24].

The precision with which the magnetic deflection is measured, i.e. the intrinsic detector resolution, dominates the resolution for  $p_T = 1$  TeV in the other areas. Multiple scattering and in the central region also energy loss fluctuations in the calorimeter limit the resolution for  $p_T = 30$  GeV.

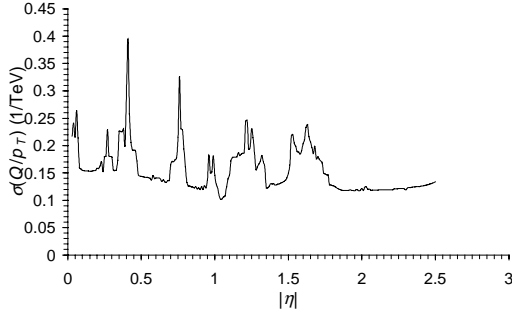


**Figure 3.43**  $\sigma(Q/p_T)$  muon spectrometer versus  $|\eta|$ , averaged over  $\phi$ ,  $p_T = 1$  TeV.

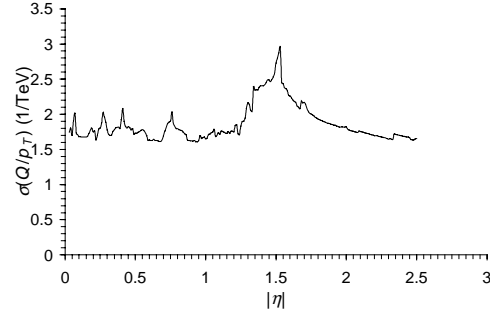


**Figure 3.44**  $\sigma(Q/p_T)$  muon spectrometer versus  $|\eta|$ , averaged over  $\phi$ ,  $p_T = 30$  GeV.

### 3.7.3 Inverse momentum resolution for the combined system

The individual track fragments reconstructed in the inner detector and muon spectrometer are combined. The square of the resolution is used as weight factor. The combined measurement of the inverse muon momentum is evaluated as:

$$k_{combined} = \frac{\sigma_{tracker}^2 k_{muon} + \sigma_{muon}^2 k_{tracker}}{\sigma_{muon}^2 + \sigma_{tracker}^2} \quad (3.40)$$

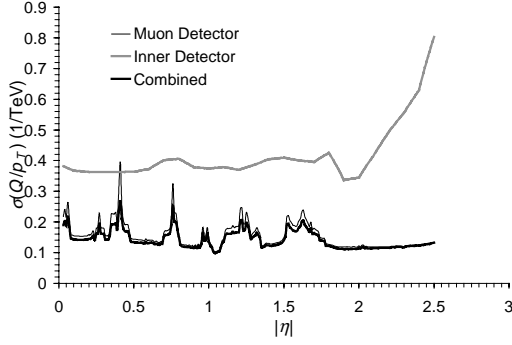
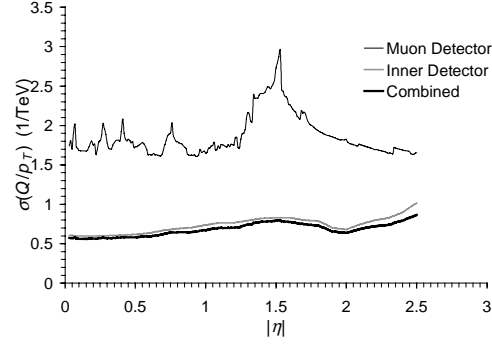
with  $k = Q/p_T$ . If  $k_{muon}$  and  $k_{tracker}$  have Gaussian errors,  $k_{combined}$  has also a Gaussian error. The resolution of the inverse momentum obtained from the combined measurement is given by<sup>10</sup>:

$$\sigma_{combined} = \frac{\sigma_{muon} \sigma_{tracker}}{\sqrt{\sigma_{muon}^2 + \sigma_{tracker}^2}} \quad (3.41)$$

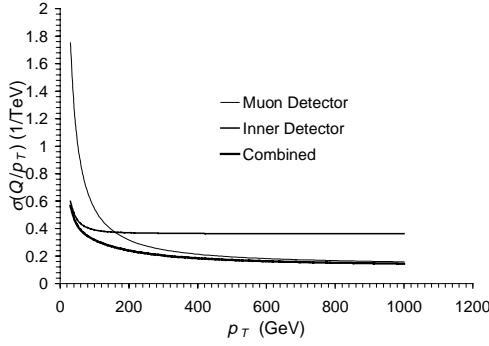
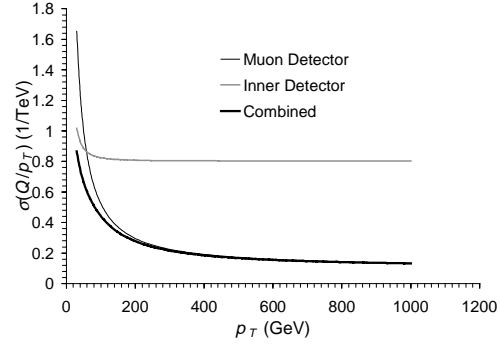
Figure 3.45 shows the inverse momentum resolution  $\sigma(Q/p_T)$  versus  $|\eta|$  for muons ( $p_T = 1$  TeV), for the inner detector alone, calculated with PRESOL, the muon detector alone (section 3.7.2, averaged over  $\phi$ ) and the combined inner detector/muon spectrometer (averaged over  $\phi$ ). The corresponding plot for  $p_T = 30$  GeV is given in figure 3.46.

For  $p_T = 1$  TeV, the inverse momentum resolution of the muon spectrometer is in general much better than the resolution of the inner detector. The performance of the muon spectrometer however fluctuates strongly in  $|\eta|$ . Above  $|\eta| = 1.75$ , the muon spectrometer almost completely determines the combined performance. Below  $|\eta| = 1.75$ , the inner detector helps to decrease the influence of the resolution fluctuations. For  $p_T = 30$  GeV (close to the lower threshold of the muon spectrometer), the inner detector almost completely determines the combined resolution.

<sup>10</sup> This expression differs from the expression used in the original implementation in ALTFast (version 1.0), where the combined performance is based on  $p_T$  and  $\sigma(p_T)$ , instead of  $k$  and  $\sigma(k)$ .

Figure 3.45  $\sigma(Q/p_T)$  versus  $|\eta|$ ,  $p_T = 1$  TeV.Figure 3.46  $\sigma(Q/p_T)$  versus  $|\eta|$ ,  $p_T = 30$  GeV.

The momentum resolution versus  $p_T$  is given in figure 3.47 ( $\eta = 0.2$ ) and figure 3.48 ( $\eta = 2.5$ ). The crossing point ( $\sigma_{\text{muon}} = \sigma_{\text{tracker}}$ ) is at about 150 GeV for small values of  $|\eta|$ . This decreases to about 50 GeV for  $|\eta| = 2.5$ .

Figure 3.47  $\sigma(Q/p_T)$  versus  $p_T$ ,  $\eta = 0.2$ .Figure 3.48  $\sigma(Q/p_T)$  versus  $p_T$ ,  $\eta = 2.5$ .

### 3.8 Muon charge identification performance

For high- $p_T$  muons, the smeared inverse momentum  $k = Q/p_T$  can have the opposite sign compared to the original inverse momentum  $\hat{k}$ . In this case misidentification of the muon charge occurs. For  $\hat{k} > 0$ , the probability for misidentification is given by<sup>11</sup>:

$$P(k \leq 0) = \frac{1}{\sqrt{2\pi}\sigma} \int_{-\infty}^0 e^{-(k' - \hat{k})^2 / 2\sigma^2} dk' = \frac{1}{\sqrt{2\pi}} \int_{-\infty}^{-\hat{k}/\sigma} e^{-t^2/2} dt = \text{erf}\left(-\hat{k}/\sigma\right) \quad (3.42)$$

A similar expression is valid for  $\hat{k} < 0$ :

$$P(k \geq 0) = \text{erf}\left(\hat{k}/\sigma\right) \quad (3.43)$$

The probability for misidentification of the muon charge as function of  $|\eta|$  for the inner detector alone is given in figure 3.49 ( $p_T = 500$  GeV) and figure 3.50 ( $p_T = 1$  TeV). The numbers are summarised in table 3.5. Especially without B-layer the charge misidentification fraction increases rapidly above  $|\eta| = 2$ . The probability of the combined system as function of  $|\eta|$  is given in figure 3.51 ( $p_T = 1$  TeV). Because for high- $p_T$  muons, the resolution of the combined system is much better than the resolution of the inner detector alone, the misidentification probability is much smaller. Due to the fluctuations in the resolution of the muon

<sup>11</sup>  $\sigma = \sigma(k)$

system, the muon charge identification performance factor fluctuates very strongly as function of  $|\eta|$ .

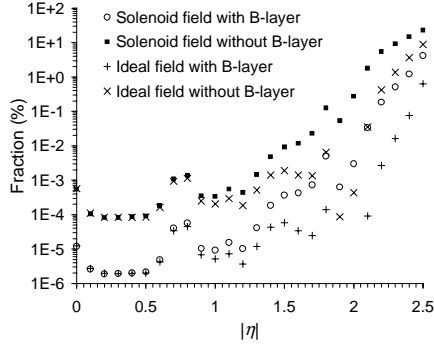


**Figure 3.49** Charge misidentification fraction [%] against  $|\eta|$  inner detector,  $p_T = 500 \text{ GeV}$ .

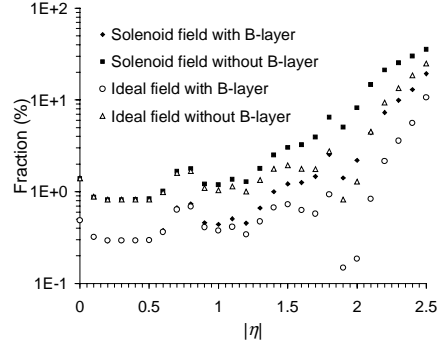


**Figure 3.50** Charge misidentification fraction [%] against  $|\eta|$ , inner detector,  $p_T = 1 \text{ TeV}$ .

**Table 3.5** The charge misidentification fraction [%] of high- $p_T$  muons in the inner detector.

$ \eta $	500 GeV				1 TeV			
	solenoid field, B-layer	solenoid field, no B-layer	ideal field, B-layer	ideal field, B-layer	solenoid field, B-layer	solenoid field, no B-layer	ideal field, B-layer	ideal field, no B-layer
0.0	$< 10^{-4}$	$5 \times 10^{-4}$	$< 10^{-4}$	$6 \times 10^{-4}$	$4.82 \times 10^{-1}$	1.38	$4.87 \times 10^{-1}$	1.40
0.1	$< 10^{-4}$	$1 \times 10^{-4}$	$< 10^{-4}$	$1 \times 10^{-4}$	$3.18 \times 10^{-1}$	$8.74 \times 10^{-1}$	$3.22 \times 10^{-1}$	$8.84 \times 10^{-1}$
0.2	$< 10^{-4}$	$1 \times 10^{-4}$	$< 10^{-4}$	$1 \times 10^{-4}$	$2.92 \times 10^{-1}$	$8.14 \times 10^{-1}$	$2.95 \times 10^{-1}$	$8.21 \times 10^{-1}$
0.3	$< 10^{-4}$	$1 \times 10^{-4}$	$< 10^{-4}$	$1 \times 10^{-4}$	$2.94 \times 10^{-1}$	$8.18 \times 10^{-1}$	$2.94 \times 10^{-1}$	$8.20 \times 10^{-1}$
0.4	$< 10^{-4}$	$1 \times 10^{-4}$	$< 10^{-4}$	$1 \times 10^{-4}$	$2.97 \times 10^{-1}$	$8.25 \times 10^{-1}$	$2.94 \times 10^{-1}$	$8.21 \times 10^{-1}$
0.5	$< 10^{-4}$	$1 \times 10^{-4}$	$< 10^{-4}$	$1 \times 10^{-4}$	$3.02 \times 10^{-1}$	$8.39 \times 10^{-1}$	$2.96 \times 10^{-1}$	$8.25 \times 10^{-1}$
0.6	$< 10^{-4}$	$2 \times 10^{-4}$	$< 10^{-4}$	$2 \times 10^{-4}$	$3.77 \times 10^{-1}$	1.01	$3.63 \times 10^{-1}$	$9.84 \times 10^{-1}$
0.7	$< 10^{-4}$	$1.1 \times 10^{-3}$	$< 10^{-4}$	$9 \times 10^{-4}$	$6.70 \times 10^{-1}$	1.66	$6.38 \times 10^{-1}$	1.60
0.8	$1 \times 10^{-4}$	$1.4 \times 10^{-3}$	$< 10^{-4}$	$1.1 \times 10^{-3}$	$7.36 \times 10^{-1}$	1.78	$6.87 \times 10^{-1}$	1.68
0.9	$< 10^{-4}$	$4 \times 10^{-4}$	$< 10^{-4}$	$2 \times 10^{-4}$	$4.59 \times 10^{-1}$	1.21	$4.10 \times 10^{-1}$	1.10
1.0	$< 10^{-4}$	$3 \times 10^{-4}$	$< 10^{-4}$	$2 \times 10^{-4}$	$4.41 \times 10^{-1}$	1.19	$3.78 \times 10^{-1}$	1.04
1.1	$< 10^{-4}$	$6 \times 10^{-4}$	$< 10^{-4}$	$3 \times 10^{-4}$	$5.07 \times 10^{-1}$	1.36	$4.14 \times 10^{-1}$	1.15
1.2	$< 10^{-4}$	$4 \times 10^{-4}$	$< 10^{-4}$	$2 \times 10^{-4}$	$4.54 \times 10^{-1}$	1.28	$3.42 \times 10^{-1}$	1.00
1.3	$< 10^{-4}$	$1.5 \times 10^{-3}$	$< 10^{-4}$	$5 \times 10^{-4}$	$6.63 \times 10^{-1}$	1.79	$4.73 \times 10^{-1}$	1.34
1.4	$2 \times 10^{-4}$	$4.8 \times 10^{-3}$	$< 10^{-4}$	$1.4 \times 10^{-3}$	1.00	2.51	$6.73 \times 10^{-1}$	1.78
1.5	$4 \times 10^{-4}$	$9.2 \times 10^{-3}$	$1 \times 10^{-4}$	$1.9 \times 10^{-3}$	1.21	3.03	$7.29 \times 10^{-1}$	1.94
1.6	$4 \times 10^{-4}$	$1.18 \times 10^{-2}$	$< 10^{-4}$	$1.4 \times 10^{-3}$	1.26	3.25	$6.29 \times 10^{-1}$	1.78
1.7	$7 \times 10^{-4}$	$2.30 \times 10^{-2}$	$< 10^{-4}$	$1.4 \times 10^{-3}$	1.47	3.94	$5.76 \times 10^{-1}$	1.76
1.8	$5.0 \times 10^{-3}$	$1.25 \times 10^{-1}$	$1 \times 10^{-4}$	$6.6 \times 10^{-3}$	2.54	6.48	$9.35 \times 10^{-1}$	2.76
1.9	$6 \times 10^{-4}$	$5.34 \times 10^{-2}$	$< 10^{-4}$	$0.1 \times 10^{-4}$	1.41	5.04	$1.49 \times 10^{-1}$	$8.22 \times 10^{-1}$
2.0	$3.0 \times 10^{-3}$	$2.73 \times 10^{-1}$	$< 10^{-4}$	$4 \times 10^{-4}$	2.20	8.19	$1.86 \times 10^{-1}$	1.29
2.1	$3.36 \times 10^{-2}$	1.80	$1 \times 10^{-4}$	$3.53 \times 10^{-2}$	4.40	14.7	$8.36 \times 10^{-1}$	4.49
2.2	$1.86 \times 10^{-1}$	5.48	$2.7 \times 10^{-3}$	$4.21 \times 10^{-1}$	7.29	21.2	2.15	9.36
2.3	$5.09 \times 10^{-1}$	9.20	$1.63 \times 10^{-2}$	1.36	9.90	25.3	3.59	13.5
2.4	1.22	14.7	$7.56 \times 10^{-2}$	3.66	13.0	30.0	5.61	18.5
2.5	4.17	22.9	$6.40 \times 10^{-1}$	8.89	19.3	35.5	10.6	25.0

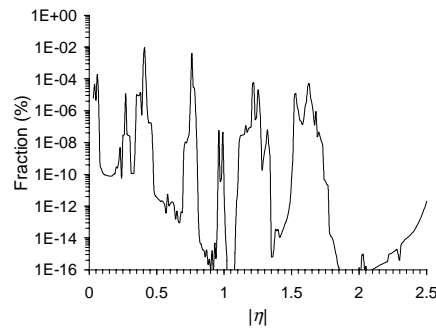


**Figure 3.51** Charge misidentification fraction [%] against  $|\eta|$ , combined system,  $p_T = 1$  TeV.

### 3.9 Principle of the description of tails

In [9] it is shown that the shape of the track parameter resolutions for pions, found with full detector simulation plus XKALMAN track reconstruction, can be described effectively by the sum of two multinormal distributions in the space of the five track parameters ( $\mathbf{p}$ ):

$$f(\mathbf{p}) = \frac{A}{(2\pi)^{2/2} \sqrt{|C|}} \exp\left(-\frac{1}{2}(\mathbf{p} - \hat{\mathbf{p}})^T C^{-1}(\mathbf{p} - \hat{\mathbf{p}})\right) + \frac{B}{(2\pi)^{2/2} \sqrt{|T|}} \exp\left(-\frac{1}{2}(\mathbf{p} - \hat{\mathbf{p}})^T T^{-1}(\mathbf{p} - \hat{\mathbf{p}})\right) \quad (3.44)$$

with  $\hat{\mathbf{p}}$  describing the unsmeared track parameters and  $\mathbf{p}$  describing the track parameters actually measured. The term  $A$  gives the fraction of the tracks in the central core (intrinsic detector resolution and multiple scattering). The term  $B = 1 - A$  gives the fraction of the tracks in the tail (e.g. scattering at large angles, track reconstruction errors). The global covariance matrix  $\mathbf{G}$  is associated to the single covariance matrices  $\mathbf{C}$  and  $\mathbf{T}$  in the following way:

$$\mathbf{G} = A\mathbf{C} + B\mathbf{T} \quad (3.45)$$

To calculate for a given set of parameters  $\hat{\mathbf{p}}$  a smeared set  $\mathbf{p}$ , it is not correct to use the global covariance matrix  $\mathbf{G}$ . Instead one of the two matrices  $\mathbf{C}$  and  $\mathbf{T}$  should be used according to the probabilities  $A$  and  $B$ . The reason is that the smearing of a track can be described either by the central core either by the tail if the track suffers from scattering at large angles or reconstruction errors. The matrix  $\mathbf{G}$  is also not a multinormal distribution that is required by the routines described in section 3.3.2.

The matrix  $\mathbf{C}$  can be calculated via the method described in section 3.4. A problem is to determine the fraction  $A$  and  $B$  and the tail covariance matrix  $\mathbf{T}$ , assuming matrix  $\mathbf{C}$  is known. In practice it is not possible to fit the full simulation data directly according to (3.44). The projection of (3.44) in the space of one track parameter  $p_i$  is given by:

$$f(p_i) = \frac{A}{\sqrt{2\pi C_{ii}}} \exp\left(-\frac{(p_i - \hat{p}_i)^2}{2C_{ii}}\right) + \frac{B}{\sqrt{2\pi T_{ii}}} \exp\left(-\frac{(p_i - \hat{p}_i)^2}{2T_{ii}}\right) \quad (3.46)$$

The model used implies that  $A$  and  $B$  are the same for each of the track parameters  $\mathbf{p}$ . In fact this assumption introduces a correlation between the  $(r, \phi)$  plane and the  $(r, z)$  plane. The fractions  $A$  and  $B$  can be determined by fitting the data found with full simulation according to this relation. Assuming that  $C_{ii}$  is known, the parameters  $A$ ,  $B$  and  $T_{ii}$  can be found via a one-dimensional least square fit with three free parameters. The average value of  $A$  and  $B$  for the five track parameters is taken as the final value.

One possible method for calculating the terms  $T_{ij}$  is via the global covariance matrix  $\mathbf{G}$ . From (3.45) it follows that  $\mathbf{T}$  is given by:

$$\mathbf{T} = \frac{\mathbf{G} - A\mathbf{C}}{B} \quad (3.47)$$

The matrix  $\mathbf{G}$  is by definition given by [18]:

$$\mathbf{G} = \sum_{i=1}^N (\mathbf{p}_i - \hat{\mathbf{p}})^T (\mathbf{p}_i - \hat{\mathbf{p}}) \quad (3.48)$$

with the numbers of tracks given by  $N$ ,  $p_i$  the measured parameters for track  $i$ , based on full detector simulation and XKALMAN reconstruction, and  $\hat{p}_i$  the original parameter for track  $i$  given by the event generator.

Another possibility to determine the correlations  $T_{ij}$  is via a least square fit, using the projection of (3.44) in the space of two parameters:

$$f(p_i, p_j) = \frac{A}{2\pi\sqrt{C_{ii}C_{jj} - C_{ij}^2}} e^{-G_1/2} + \frac{B}{2\pi\sqrt{T_{ii}T_{jj} - T_{ij}^2}} e^{-G_2/2} \quad (3.49)$$

with  $G_1$  and  $G_2$  given by:

$$\begin{aligned} G_1 &= \frac{C_{ii}C_{jj}}{C_{ii}C_{jj} - C_{ij}^2} \left[ \frac{(p_i - \hat{p}_i)^2}{C_{ii}} - 2\frac{C_{ij}}{C_{ii}C_{jj}}(p_i - \hat{p}_i)(p_j - \hat{p}_j) + \frac{(p_j - \hat{p}_j)^2}{C_{jj}} \right] \\ G_2 &= \frac{T_{ii}T_{jj}}{T_{ii}T_{jj} - T_{ij}^2} \left[ \frac{(p_i - \hat{p}_i)^2}{T_{ii}} - 2\frac{T_{ij}}{T_{ii}T_{jj}}(p_i - \hat{p}_i)(p_j - \hat{p}_j) + \frac{(p_j - \hat{p}_j)^2}{T_{jj}} \right] \end{aligned} \quad (3.50)$$

Assuming that  $A$ ,  $B$ ,  $C_{ii}$ ,  $C_{ij}$  and  $T_{ii}$  are known, the term  $T_{ij}$  can be found by fitting the full simulation data according to this relation.

A slightly different method is suggested in [9] and implemented in the current ATLFASST version. The parameters  $A$ ,  $B$ ,  $C_{11}$  and  $T_{11}$  are determined using (3.46) for the transverse impact parameter only. The term  $C_{11}$  is also used as fit parameter. It is assumed that  $A$  and  $B$  are the same for the other parameters. The tail covariance matrix  $\mathbf{T}$  is determined using (3.47). The calculation of  $\mathbf{C}$  is not based on the method described in section 3.3.2. The XKALMAN algorithm gives for each track a complete  $5 \times 5$  covariance matrix  $\mathbf{X}$ . In this matrix, multiple scattering and bremsstrahlung energy losses are taken into account. The matrix  $\mathbf{C}$  is calculated from this matrix  $\mathbf{X}$  (averaged over all tracks), using the term  $C_{11}$  found in the transverse impact parameter fit as weight factor:

$$C_{ij} = X_{ij} \frac{C_{11}}{X_{11}} \quad (3.51)$$

### 3.10 Conclusions and further work

In this chapter it has been shown that the performance of the inner detector for muon tracks can very effectively be parameterised as function of  $p_T$  and  $|\eta|$  taking into account both the intrinsic detector resolution and multiple scattering. The parameterisation can easily be extended to include track reconstruction inefficiencies. To include track reconstruction inefficiencies a Boolean function can be used returning yes if the current track is reconstructed and no else. This decision is based on a probability distribution.

In the previous section an empirical method is described to include tails (due to for example track reconstruction errors) in the parameterisation. A correct description of tails is important for the parameterisation of the inner detector performance for pion and electron tracks. More work is necessary in this area.

The current parameterisation is especially useful for physics channels with isolated high- $p_T$  leptons, e.g. SUSY physics described in the next chapter. The parameterisation is probably of very limited use for B-physics studies where secondary pions and the reconstruction of secondary vertices are important.



### 3.11 References

1. E.J. Buis, R.J. Dankers, A. Reichold and S.J. Haywood, *Parameterisation of the Inner Detector Performance*, ATLAS INDET-NO-195 (1997).
2. E. Richter-Was, D. Froidevaux and L. Poggioli, *ATLFAST 1.0, a Package for Particle Level Analysis*, ATLAS PHYS-NO-079 (1996).
3. R. Brun and E. Richter-Was, *Getting Started with ATLFAST++, a Fast Simulation for ATLFAST: OO/C++ Implementation*, [http://www.root.cern.ch/root/html/atlfast/USER\\_index.html](http://www.root.cern.ch/root/html/atlfast/USER_index.html), 1997.
4. R. Brun et al., *GEANT3*, CERN DD/EE/84-1 (1986).
5. A. Artamonov, A. Dell'Acqua, D. Froidevaux, M. Nessi, P. Nevski and G. Poulard, *DICE-95*, ATLAS-SOFT/94-14c (1996).
6. I. Gavrilenko, P.N. Lebedev, *XKALMAN Algorithm Description*, ATLAS INDET-DRAFT, 1996.
7. F.E. Paige, *Precision SUSY Measurements with ATLAS: Simulation Tools and Inclusive Analysis*, Transparencies presented at LHCC SUSY workshop, 1996.
8. CERN Computing and Networks Division, CERN Program Library Short Write-ups, 1995.
9. F. Tartarelli and N. Labanca, *Parameterisations for ATLFAST*, Presentation given at ATLAS B-physics meeting of 18 November 1997.
10. A. Poppleton, Source code of PRESOL.
11. ATLAS Inner Detector Community, *Inner Detector Technical Design Report Volume 1*, ATLAS TDR-4, CERN/LHCC 97-16 (1997).
12. A. Reichold, Private communication.
13. A. Poppleton, Subroutine GEOM in source code of PRESOL.
14. ATLAS Inner Detector Community, *Inner Detector Technical Design Report Volume 2*, ATLAS TDR-5, CERN/LHCC 97-17 (1997).
15. V.I. Klyukhin, A. Poppleton and J. Schmitz, *Field Integrals for the ATLAS Tracking Volume*, ATLAS INDET-NO-23 (1993).
16. Particle data group, *Review of Particle Properties*, Physical Review D54, 1 (1996).
17. S.J. Haywood, *Helix Fits with Stereo Measurements*, ATLAS INDET-NO-095 (1995).
18. W.J. Metzger, *Statistical Methods in Data Analysis*, Experimental High Energy Physics Group Nijmegen, HEN-343 (1996).
19. S.J. Haywood, *Impact Parameter Resolution in the Presence of Multiple Scattering*, ATLAS INDET-NO-091 (1995).
20. M. Virchaux and L. Chevalier, Subroutine RESOLUMU in source code of ATLFAST.
21. M. Virchaux and L. Chevalier, Subroutine DELOSMU in source code of ATLFAST.
22. M. Virchaux and L. Chevalier, Subroutine RESOLUMU\_BIS in source code of ATLFAST.
23. ATLAS Muon Spectrometer Community, *ATLAS Muon Spectrometer Technical Design Report*, CERN/LHCC 97-22 (1997).
24. ATLAS Magnet Project Collaboration, *ATLAS Magnet System Technical Design Report*, ATLAS TDR-6, CERN/LHCC 97-18 (1997).

